Modelling Cycles in Climate Series: the Fractional Sinusoidal Waveform Process

Tommaso Proietti *
Università di Roma "Tor Vergata"

Federico Maddanu
Università di Roma "Tor Vergata"

Abstract

The paper proposes a novel model for time series displaying persistent stationary cycles, the fractional sinusoidal waveform process. The underlying idea is to allow the parameters that regulate the amplitude and phase to evolve according to fractional noise processes. Its advantages with respect to popular alternative specifications, such as the Gegenbauer process, are twofold: the autocovariance function is available in closed form, which opens the way to exact maximum likelihood estimation; secondly the model encompasses deterministic cycles, so that discrete spectra arise as a limiting case. A generalization of the process, featuring multiple components, an additive 'red noise' component and exogenous variables, provides a model for climate time series with mixed spectra. Our illustrations deal with the change in amplitude and phase of the intra-annual component of carbon dioxide concentrations in Mauna Loa, and with the estimation and the quantification of the contribution of orbital cycles to the variability of paleoclimate time series.

Keywords: Mixed Spectrum. Cyclical long memory. Paleoclimatic data.

*Address for Correspondence: Università di Roma "Tor Vergata", Dipartimento di Economia e Finanza, Via Columbia 2, 00133 Roma, Italy. Email: tommaso.proietti@uniroma2.it.

1 Introduction

Climate time series are characterized by persistent periodic or quasi-periodic movements. In reconstructed paleoclimate proxy records these are commonly referred to as glacial cycles. In the analysis of subannual time series dealing with temperatures and trace gases concentrations, the propagation of daily or annual insolation forcing arising from Earth's rotation through the different parts of the climate system and their interactions can originate seasonal cycles characterized by time varying amplitude and phases.

In modelling cycles, an important dichotomy is between deterministic cycles and stochastic ones. The former are characterized by a purely discrete (or line) spectrum; see, e.g., Brockwell and Davis (1991, section 4.2). An example is the harmonic process $\{y_t, t \in \mathbb{Z}, y_t \in \mathbb{R}\}$ defined as $y_t = \alpha \cos(\lambda t) + \alpha^* \sin(\lambda t)$, where λ is a known frequency in $[0, \pi]$ and α, α^* are mutually independent Gaussian random variables with mean zero and variance σ_α^2.

Stochastic cycles are further characterized by their stationarity and their memory. The second order autoregressive process $y_t = 2\rho\cos(\lambda)y_{t-1} - \rho^2 y_{t-2} + \varepsilon_t, \varepsilon_t \sim$ i.i.d. $\mathrm{N}(0, \sigma^2)$, with $|\rho| < 1$, is a model for a short memory cycle, and it is such that the spectral density is continuous and bounded, with a spectral peak around the frequency λ. If $\rho = 1$ the cycle is nonstationary and it is said to be integrated of order 1 at the frequency λ. Introducing the lag operator L, $L^k y_t = y_{t-k}, k \in \mathbb{Z}$, the integrated cycle is written $(1 - 2\cos(\lambda)L + L^2)y_t = \varepsilon_t$.

An important model for cyclical long memory time series is the Gegenbauer processes, introduced by Hosking (1981) and formalized by Andel (1986) and Gray et al. (1989). The Gaussian Gegenbauer process $\{y_t, t \in \mathbb{Z}, y_t \in \mathbb{R}\}$ is defined by the following dynamic equation,

$$\left(1 - 2\cos(\lambda)L + L^2\right)^d y_t = \varepsilon_t,$$

where $d \in \mathbb{R}$ is the memory parameter. The process is stationary if $0 < \lambda < \pi$ and $d < 1/2$, or when $\lambda = 0, \pi$ and $d < 1/4$; its spectral density, $f(\omega)$, for $-\pi \leq \omega \leq \pi$, is

$$f(\omega) = \frac{\sigma^2}{2\pi} \left|2\sin\left(\frac{\omega - \lambda}{2}\right)\right|^{-2d} \left|2\sin\left(\frac{\omega + \lambda}{2}\right)\right|^{-2d}.$$

and has poles at the frequencies $\pm\lambda$.

Gray et al. (1989) generalized the process to the case when ϵ_t is an autoregressive moving average (ARMA) process; Giraitis and Leipus (1995) and Woodward et al. (1998) introduced the k-factor Gegenbauer ARMA (k-GARMA) model, which allows for multiple periodicity and poles in the spectral density. Other classes of seasonal long-range dependent models have been proposed by Porter-Hudak (1990), Hassler (1994), and Koopman et al. (2007).

As for inference about the model parameters, essential references are Chung (1996b, 1996a), Hosoya (1997), Arteche and Robinson (2000), Giraitis et al. (2001) and Palma and Chan (2005). Robinson (1994) proposes a test of cyclical and seasonal nonstationarity and Dalla and Hidalgo (2005) propose a test of the hypothesis of long memory versus short memory cycles. Recently, Leschinski and Sibbertsen (2019) have dealt with the problem

of selecting the number of cyclical components in the k-GARMA model. Ferrara and Guégan (2001) deal with forecasting.

Several applications in economics and financial econometrics are available, see Bisaglia et al. (2003) and Bordignon et al. (2007), among others. For applications to climatological time series, see Gil-Alana (2017). The literature is indeed very large and we refer to Palma (2007, ch. 12), Surgailis et al. (2012, ch. 7), Woodward et al. (2017, ch. 11) and Dissanayake et al. (2018) for reviews and discussions.

One limitation of the Gegenbauer process and its generalizations is the lack of a closed form expression for the autocovariance function. This prevents exact maximum likelihood estimation and optimal signal extraction, and only approximate inferences are available. To address this issue, efficient computational techniques for evaluating the Gegenbauer autocovariance have been proposed in the literature by Lapsa (1997), McElroy and Holan (2012) and McElroy and Holan (2016). A minor issue is the discontinuity in the order of fractional integration at the long run and Nyquist frequencies. Finally, the k-factor Gegenbauer model is a reduced-form multiplicative model which does not allow the measurement of the contribution of the components of variability at different cycle frequencies[1], which is one the aims of our analysis of climate time series.

We propose an additive approach which combines independent persistent cycles generated by a novel process, the fractional Sinusoidal Waveform (fSW) process. The latter is defined by the modulation of the trigonometric functions, $\cos(\lambda t)$ and $\sin(\lambda t)$, by two independent fractional noise processes, with the same memory and variance, which replace the random coefficients α and α^* in the above harmonic process. This is similar in spirit to the class of integrated cycle models defined by Hannan (1964), who considered modulation by random walk processes. As a result, both amplitude and phase vary stochastically, with persistence in their movements, regulated by the memory parameter.

As will be shown in the paper, when the process is stationary, the autocovariance function is available as the product of the autocovariance sequence of the fractional noise process and a cosine sequence defined at the cyclical frequency. Assuming Gaussianity, this opens the way to the estimation of the model parameters by maximum likelihood, the exact likelihood being evaluated with the support of the Durbin-Levinson recursions. The fSW process can also be obtained as the sum of two complex coniugate fractional noise processes, which allow the derivation of the spectral density in closed form. Furthermore, a direct extensions of the argument adopted by Granger (1980) allows to prove that cyclical long memory can originate from the contemporaneous aggregation of short memory cyclical processes.

For the analysis of cycles and seasonality in climate time series we propose an additive generalization of the fSW model, resulting from the linear combination of independent fSW processes. For capturing the low frequency movements, a *red noise* component is added. The latter is meant to capture the internal variability of the climate system, whereas the fSW cyclical components are used to capture the variability due to external forcing; see Mitchell (1976). The introduction of fixed regression effects completes the

[1] Although Beveridge-Nelson type decompositions can in principle be defined, see Proietti (2016) for the zero frequency, no general theory is available for this purpose.

specification of the model. An important question for climate time series is the treatment of mixed spectra, featuring deterministic cyclical components embedded in a background continuum (see Mann and Lees (1996) and Meyers et al. (2008)). An additional important property of the fSW is the possibility to encompass stationary deterministic cycles, i.e., a process with discrete spectrum, which arise as a limiting case of our basic fSW process. Also, minimum mean square signal extraction analytical formulae are available for the measurement of the components of variability.

Our illustrations deal with the characterization of the sources of variability of carbon dioxide concentrations at Manua Loa. Among the interpretative challenges posed by the Mauna Loa series, we focus on the quantification of the changes of the amplitude and phase of the seasonal cycle, which are one possible manifestations of how climate change affects the carbon cycle, and the relation of the interannual component with the El Niño Southern Oscillation phenomenon. A second application deals with the estimation and the quantification of the contribution of orbital cycles to the variability of paleoclimate time series.

The paper is organized as follows. In section 2 we introduce the fractional sinusoidal waveform model, and present its essential properties: using the linear process represention, we derive its autocovariance function. The fSW process can also be expressed as the sum of two complex coniugate fractional noise processes, which allows an easy derivation of the spectral density function (section 2.2). Section 2.3 shows that deterministic cycles arise as a limiting case. Section 3 shows that cyclical long memory can result from the contemporaneous aggregation of stationary short memory cyclical processes.

In section 4 we consider a more general specification which features multiple fSW cycles, as well as a *red noise*, or background low-frequency component and a regression component.

Maximum likelihood inference, both exact and using the Whittle approximation, and optimal signal extraction are the topic of section 5. Our climatological illustrations deal with assessing the inter-annual and intra-annual variability of carbon dioxide (CO_2) concentrations at Mauna Loa (section 6) and measuring the contribution of orbital forcing to paleoclimate variability of temperatures, ice volume, methane and CO_2 and more generally to glacial cycles (section 7). Section 8 concludes the paper.

2 The Fractional Sinusoidal Waveform process

The Gaussian process $\{y_t, t \in \mathbb{Z}\}$ defined below is a fractional Sinusoidal Waveform process with memory parameter d, frequency λ and disturbance variance σ_η^2:

$$\begin{array}{rcll} y_t & = & \alpha_t \cos(\lambda t) + \alpha_t^* \sin(\lambda t), & t \in \mathbb{Z}, \\ \alpha_t & = & (1-L)^{-d}\eta_t, & \eta_t \sim \text{i.i.d. } \mathrm{N}(0, \sigma_\eta^2), \\ \alpha_t^* & = & (1-L)^{-d}\eta_t^*, & \eta_t^* \sim \text{i.i.d. } \mathrm{N}(0, \sigma_\eta^2), \end{array} \tag{1}$$

where η_t and η_t^* are mutually independent.

The process (1) is stationary when $d < 1/2$, in which case $\mathrm{E}(y_t) = 0$, $\mathrm{Var}(y_t) \equiv \sigma_\alpha^2$, with $\sigma_\alpha^2 = \sigma_\eta^2 \frac{\Gamma(1-2d)}{\Gamma^2(1-d)}$. The autocovariance function, $\gamma(k) = \mathrm{E}(y_t y_{t-k})$, takes the form

$$\gamma(k) = \sigma_\eta^2 \frac{\Gamma(1-2d)\Gamma(d+k)}{\Gamma(1+k-d)\Gamma(d)\Gamma(1-d)} \cos(\lambda k), \quad k \in \mathbb{Z}, \tag{2}$$

as will be shown in section 2.1.

The spectral density function is derived in section 2.2:

$$f(\omega) = \frac{\sigma_\eta^2}{4\pi} \left\{ \left| 2\sin\left(\frac{\omega-\lambda}{2}\right) \right|^{-2d} + \left| 2\sin\left(\frac{\omega+\lambda}{2}\right) \right|^{-2d} \right\}, \omega \in [-\pi, \pi]. \tag{3}$$

The fSW can equivalently be written $y_t = A_t \cos(\lambda t - \varphi_t)$, where $A_t = \sqrt{\alpha_t^2 + \alpha_t^{*2}}$ is the random amplitude, with marginal Rayleigh distribution with $\mathrm{E}(A_t) = \sigma_\alpha \sqrt{\pi/2}$ and $\mathrm{Var}(A_t) = \sigma_\alpha^2(2 - \pi/2)$, while the random phase is $\varphi_t = \arctan(\alpha_t^*/\alpha_t) \sim U(-\pi, \pi)$.

Figure 1 displays the time series plot of a simulated realization of length $n = 500$, generated by a fSW process with $d = 0.40$, $\lambda = \pi/6$, $\sigma_\eta^2 = 1$, its sample autocorrelation function, and periodogram.

2.1 Linear process representation and autocovariance function

Let us consider the case when $d < 1/2$ and $\sigma_\eta^2 > 0$. Using the binomial expansion

$$(1-L)^{-d} = \sum_{j=0}^{\infty} \psi_j L^j, \;\; \psi_j = \frac{\Gamma(j+d)}{\Gamma(j+1)\Gamma(d)}, j = 0, 1, \ldots,$$

where $\Gamma(\cdot)$ is the Gamma function, and setting $\mathbf{z}_t = [\cos(\lambda t), \sin(\lambda t)]'$, $\boldsymbol{\alpha}_t = [\alpha_t, \alpha_t^*]'$,

$$\begin{array}{rcl} y_t & = & \mathbf{z}_t' \boldsymbol{\alpha}_t \\ & = & \mathbf{z}_t' \sum_{j=0}^{\infty} \psi_j \boldsymbol{\eta}_{t-j} \\ & = & \sum_{j=0}^{\infty} \psi_j \mathbf{z}_0' \mathbf{C}^j \boldsymbol{\kappa}_{t-j} \\ & = & \sum_{j=0}^{\infty} \psi_j \cos(\lambda j) \kappa_{t-j} + \sum_{j=0}^{\infty} \psi_j \sin(\lambda j) \kappa_{t-j}^*, \end{array} \tag{4}$$

where $\boldsymbol{\eta}_t = [\eta_t, \eta_t^*]'$; the third line follows from writing $\mathbf{z}_t = \mathbf{C}^{t'} \mathbf{z}_0$, with $\mathbf{z}_0 = \begin{bmatrix} 1 & 0 \end{bmatrix}'$,

$$\mathbf{C} = \begin{bmatrix} \cos(\lambda) & \sin(\lambda) \\ -\sin(\lambda) & \cos(\lambda) \end{bmatrix}$$

is the orthogonal Givens rotation matrix with angle λ, and $\boldsymbol{\kappa}_t = [\kappa_t, \kappa_t^*]$ is defined as $\boldsymbol{\kappa}_t = \mathbf{C}^t \boldsymbol{\eta}_t$. Notice that $\mathrm{E}(\boldsymbol{\kappa}_t \boldsymbol{\kappa}_t') = \sigma_\eta^2 \mathbf{I}$.

The autocovariance function of the fractional noise process follows from Hosking (1981, Theorem 1). Let $\gamma_\alpha(k)$ denote the autocovariance function of the scalar fractional noise process $(1-L)^d \alpha_t = \eta_t$,

$$\begin{array}{rcl} \gamma_\alpha(k) & = & \sigma_\eta^2 \sum_{j=0}^{\infty} \psi_j \psi_{j+k} \\ & = & \sigma_\eta^2 \frac{(-1)^k \Gamma(1-2d)}{\Gamma(k+1-d)\Gamma(-k+1-d)}, \end{array}$$

Figure 1: Simulated time series of length $n = 500$, generated by an fSW process with $d = 0.40$, $\lambda = \pi/6$, $\sigma_\eta^2 = 1$. The middle plot is its sample autocorrelation. The bottom panel plots the periodogram and the theoretical spectral density.

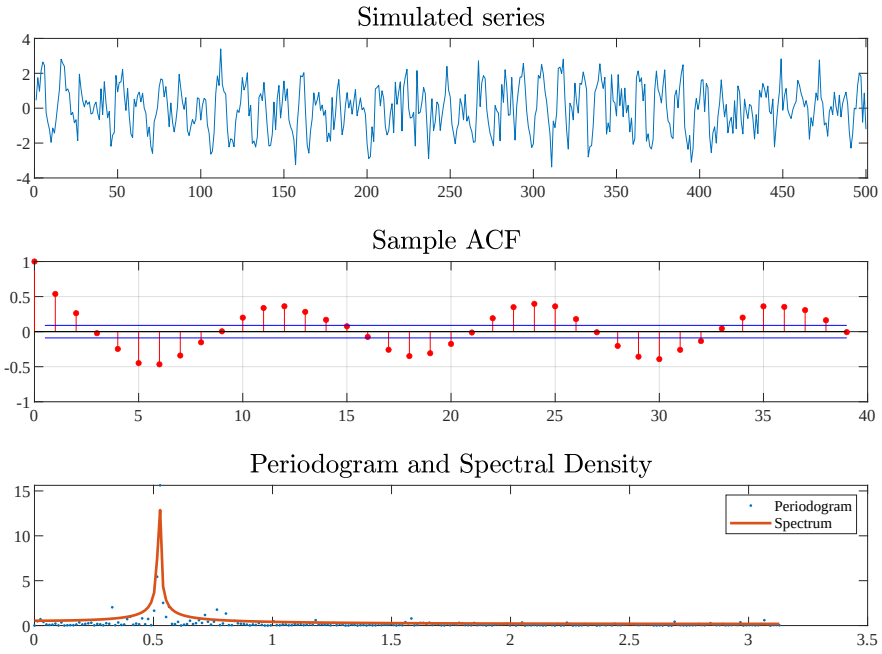

see, e.g. Beran et al. (2016), page 49. Then, the autocovariance function of y_t takes the form:

$$\begin{aligned}\gamma(k) &= \sigma_\eta^2 \sum_{j=0}^{\infty} \psi_j \psi_{j+k} \mathbf{z}_t' \mathbf{z}_{t-k} \\ &= \gamma_\alpha(k) \cos(\lambda k) \\ &= \sigma_\eta^2 \frac{(-1)^k \Gamma(1-2d)}{\Gamma(1-d+k)\Gamma(1-d-k)} \cos(\lambda k) \\ &= \sigma_\eta^2 \frac{\Gamma(1-2d)\Gamma(d+k)}{\Gamma(1-d+k)\Gamma(d)\Gamma(1-d)} \cos(\lambda k)\end{aligned}$$

as stated in (2), where the last line follows from Euler's reflection formula.

The autocorrelation function is $\rho(k) = \sigma_\alpha^{-2}\gamma(k)$,

$$\rho(k) = \frac{\Gamma(1-d)\Gamma(d+k)}{\Gamma(1-d+k)\Gamma(d)} \cos(\lambda k), k \in \mathbb{Z}.$$

As $k \to \infty$, $\rho(k) \sim ck^{2d-1}\cos(k\lambda)$, $c > 0$, an hyperbolically damped cosine wave, as it is implied by Sterling's approximation $\frac{\Gamma(d+k)}{\Gamma(1-d+k)} \sim k^{2d-1}$. Hence, the process features cyclical long memory in the sense specified by Oppenheim and Viano (2004).

2.2 Complex fractional noise representation and spectral density

An alternative representation can be obtained by considering the complex fractional noise process

$$(1 - e^{-\imath\lambda}L)^d w_t = \zeta_t, \quad \lambda \in [0, \pi]$$

where ζ_t is a complex Gaussian white noise process with independent real and imaginary part, $\zeta_t = 2^{-1/2}(\kappa_t + \imath\kappa_t^*)$, with κ_t and κ_t^* i.i.d. Gaussian variables, defined in the previous section, so that $\mathrm{Var}(\zeta_t) = \sigma_\kappa^2$ and, denoting $\bar{\zeta}_t = 2^{-1/2}(\kappa_t - \imath\kappa_t^*)$, $\mathrm{Cov}(\zeta_t, \bar{\zeta}_t) = 0$. Let $\bar{w}_t$ denote the complex conjugate fractional noise process $(1 - e^{\imath\lambda}L)^d \bar{w}_t = \bar{\zeta}_t$.

Using the binomial expansion $(1 - e^{-\imath\lambda}L)^{-d} = \sum_{j=0}^{\infty} \psi_j e^{-\imath\lambda j} L^j$

$$\begin{array}{rcl} y_t & = & \frac{1}{\sqrt{2}}(w_t + \bar{w}_t) \\ & = & \frac{1}{\sqrt{2}}\left\{(1 - e^{-\imath\lambda}L)^{-d}\zeta_t + (1 - e^{\imath\lambda}L)^{-d}\bar{\zeta}_t\right\} \\ & = & \frac{1}{\sqrt{2}}\sum_{j=0}^{\infty}\psi_j\left\{e^{-\imath\lambda j}\zeta_{t-j} + e^{\imath\lambda j}\bar{\zeta}_{t-j}\right\} \\ & = & \sum_{j=0}^{\infty}\psi_j\cos(\lambda j)\kappa_{t-j} + \sum_{j=0}^{\infty}\psi_j\sin(\lambda j)\kappa_{t-j}^*. \end{array} \tag{5}$$

Notice that the last line of (5) coincides with (4); therefore, $y_t = \frac{1}{\sqrt{2}}(w_t + \bar{w}_t)$ is a fSW process. Also, rewriting the second line of (5) as

$$y_t = \frac{1}{\sqrt{2}}\frac{(1-e^{\imath\lambda}L)^d\zeta_t + (1-e^{-\imath\lambda}L)^d\bar{\zeta}_t}{(1-2\cos\lambda L + L^2)^d}, \tag{6}$$

we see that y_t has an infinite autoregressive feature generated by the fractional Gegenbauer polynomial in the denominator of (6).

Defining now the process y_t^*

$$\begin{array}{rcl} y_t^* & = & \frac{\imath}{\sqrt{2}}(\bar{w}_t - w_t) \\ & = & -\sum_{j=0}^{\infty}\psi_j\sin(\lambda j)\kappa_{t-j} + \sum_{j=0}^{\infty}\psi_j\cos(\lambda j)\kappa_{t-j}^*, \end{array}$$

where the second line is derived similarly to (5), we have

$$\begin{bmatrix} y_t \\ y_t^* \end{bmatrix} = \sum_{j=0}^{\infty}\psi_j\mathbf{C}^j\boldsymbol{\kappa}_{t-j},$$

which for $d = 1$ reduces to the Markov process $(\mathbf{I} - \mathbf{C}L)[y_t, y_t^*]' = \boldsymbol{\kappa}_t$, and both y_t and y_t^* are real processes.

The spectral density is obtained directly from replacing L in (6) by $e^{-\imath\omega}$, giving (3). Writing

$$f(\omega) = \frac{\sigma_\eta^2}{4\pi}|\omega - \lambda|^{-2d}\left\{\left|\frac{\sin\left(\frac{\omega-\lambda}{2}\right)}{\frac{\omega-\lambda}{2}}\right|^{-2d} + \left|\frac{\frac{\omega-\lambda}{2}}{\sin\left(\frac{\omega+\lambda}{2}\right)}\right|^{2d}\right\},$$

shows that $f(\omega) \sim \frac{\sigma_\eta^2}{4\pi}|\omega - \lambda|^{-2d}$ as $\omega \to \lambda$.

2.3 Deterministic cycles

The harmonic process $y_t = \alpha\cos(\lambda t) + \alpha^*\sin(\lambda t)$, where α and α^* are independent and identically distributed Gaussian random variables with mean zero and variance σ_α^2, is a model for a stationary deterministic cycle, characterized by the autocovariance function $\mathrm{Cov}(y_t, y_{t-k}) = \sigma_\alpha^2\cos(\lambda k)$, $k \in \mathbb{Z}$, and discrete spectrum with point mass $\sigma_\alpha^2/(2\pi)$ at the frequencies $\pm\lambda$.

Let us consider again the general expression (2) for the autocovariance function of the fSW process, and recall $\sigma_\alpha^2 = \sigma_\eta^2 \frac{\Gamma(1-2d)}{\Gamma^2(1-d)}$. Assume that for a positive constant c we can write $\sigma_\eta^2 = 4c(1-2d)/\pi$. Then, if $d \to \frac{1}{2}$ from the left, $\lim_{d\to\frac{1}{2}-}\sigma_\alpha^2 = c > 0$ (as $\lim_{x\to 0^+} x\Gamma(x) = 1, x = 1-2d,$). Moreover, the autocovariance function

$$\gamma(k) = \sigma_\alpha^2 \frac{\Gamma(1-d)\Gamma(d+k)}{\Gamma(1+k-d)\Gamma(d)}\cos(\lambda k), \sigma_\alpha^2 > 0,$$

for $d \to (1/2)^-$, tends to $\gamma(k) = \sigma_\alpha^2\cos(\lambda k)$. Hence, when $\sigma_\eta^2 \to 0$ and $d \to \frac{1}{2}$ from the left, the fSW process has the same autocovariance function of a harmonic process.

Also, writing the spectral density function (3) in terms of σ_α^2,

$$f(\omega) = \frac{\sigma_\alpha^2}{4\pi}\frac{\Gamma^2(1-d)}{\Gamma(1-2d)}\left\{\left|2\sin\left(\frac{\omega-\lambda}{2}\right)\right|^{-2d} + \left|2\sin\left(\frac{\omega+\lambda}{2}\right)\right|^{-2d}\right\}, \omega \in [-\pi, \pi],$$

$\lim_{d\to\frac{1}{2}-} f(\omega) = \frac{\sigma_\alpha^2}{2}\delta(\omega-\lambda)$, where $\delta(\cdot)$ is Dirac's Delta function. Hence, the spectral density degenerates to a point with mass $\sigma_\alpha^2/2$ at $\omega = \pm\lambda$ and is 0 elsewhere.

3 Contemporaneous aggregation and cyclical long memory

Granger (1980) has shown that long memory can originate from the contemporaneous aggregation of heterogeneous short memory AR(1) processes. This result has been extended in various directions, see, among others, Gonçalves and Gourieroux (1988), Abadir and Talmain (2002), Davidson and Sibbertsen (2005), Schennach (2018); Oppenheim and Viano (2004) consider the aggregation of higher order autoregressive processes. Lippi and Zaffaroni (1998) and Haldrup and Vera-Valdés (2017) have extended Granger's result to other definitions of long memory.

We iterate the argument by Granger (1980) to illustrate a possible generating mechanism for cyclical long memory. Let us consider a panel of N cyclical processes,

$$y_{it} = \alpha_{it}\cos(\lambda t) + \alpha_{it}^*\sin(\lambda t), \quad i = 1, 2, \ldots, N,$$

where $\lambda \in [0, \pi]$ is a fixed frequency and the coefficients follow independent AR(1) processes $\alpha_{it} = \phi_i\alpha_{i,t-1} + \eta_{it}$, $\eta_{it} \sim$ i.i.d. $\mathrm{N}(0, \sigma_\eta^2)$, $\alpha_{it}^* = \phi_i\alpha_{i,t-1}^* + \eta_{it}^*$, $\eta_{it}^* \sim$ i.i.d. $\mathrm{N}(0, \sigma_\eta^2)$ (with little loss of generality we assume that the disturbance variance σ_η^2 is common and invariant to i).

The individual coefficients ϕ_i^2 are an i.i.d. sample from a Beta distribution, $\phi^2 \sim \text{Beta}(p,q)$, so that the probability density function of ϕ is

$$g(\phi) = \frac{2}{B(p,q)}\phi^{2p-1}(1-\phi^2)^{q-1}, \quad \phi \in (0,1), p, q > 1,$$

where $B(p,q) = \Gamma(p)\Gamma(q)/\Gamma(p+q)$. If the process y_{it} has started in the indefinite past, then its autocovariance function is

$$\gamma_i(k) = \sigma_\eta^2 \frac{\phi_i^k}{1-\phi_i^2}\cos(\lambda k).$$

We are interested in characterizing the behaviour of cross-sectional aggregate

$$y_{Nt} = \frac{1}{\sqrt{N}}\sum_{i=1}^{N} y_{it},$$

whose autocovariance function $\gamma_N(k) = \text{E}(y_t y_{t-k})$ is $\gamma_N(k) = \frac{1}{N}\sum_{i=1}^{N}\gamma_i(k), k \in \mathbb{Z}$. By the law of large numbers

$$\begin{aligned}
\lim_{N\to\infty}\gamma_N(k) &= \sigma_\eta^2 \text{E}_\phi\left(\tfrac{\phi_i^k}{1-\phi_i^2}\right)\cos(\lambda k) \\
&= \sigma_\eta^2 \tfrac{B(p+k/2,q-1)}{B(p,q)}\cos(\lambda k) \\
&\approx \sigma_\eta^2 \tfrac{\Gamma(q-1)}{B(p,q)} k^{1-q}\cos(\lambda k), \qquad k \to \infty,
\end{aligned}$$

where the last line follows by Stirling's approximation. Hence, y_{Nt} displays long memory with parameter $d = 1 - q/2$ in the covariance sense at the frequency λ.

To prove that the limiting spectral density of y_{Nt} has poles at the frequencies $\pm\lambda$ we start by writing $y_{it} = 2^{-1/2}(w_{it} + \bar{w}_{it})$, with w_{it} is the idiosyncratic complex AR(1) process $(1-\phi_i e^{-\imath\lambda}L)w_{it} = \zeta_{it}$, and $\zeta_{it} = (\kappa_{it} + \imath\kappa_{it}^*)/\sqrt{2}$, where κ_{it} κ_{it}^* are *i.i.d.* Gaussian white noises with common variance σ_η^2. The spectral density of the disaggregate process y_{it} is then

$$f_i(\omega) = \frac{\sigma_\eta^2}{4\pi}\left\{\frac{1}{|1-\phi_i e^{-\imath(\omega+\lambda)}|^2} + \frac{1}{|1-\phi_i e^{-\imath(\omega-\lambda)}|^2}\right\}$$

Then, Lemma 2 in Oppenheim and Viano (2004), is used to show that $f_N(\omega) = N^{-1}\sum_{i=1}^{N} f_i(\omega)$, has poles at the frequencies $\pm\lambda$ of order $|\omega-\lambda|^{-q}$ $(\omega \to \lambda)$, as N tends to infinity. Alternatively, we could use the series expansion of $|1-\phi_i e^{-\imath(\omega-\lambda)}|^{-2}$ as in Granger (1980).

4 Multiple periodicities, red noise and explanatory variables

Multiple periodic components arise when different cycles are present or when harmonic components are included. In the latter case, if λ_1 denotes the fundamental frequency of a cyclical component with period $s = 2\pi/\lambda_1$, the harmonic frequencies are $\lambda_j = \lambda_1 j, j = 2, \ldots, \lfloor s/2 \rfloor$.

The spectrum of climate time series, due to orbital forcing (which in general can include the annual solar cycle), has mixed nature, resulting from a combination of discrete spectral lines and continuous components. A general presentation of processes with mixed spectra is provided by Quinn and Hannan (2001), Li (2013) and Percival and Walden (2020, ch. 10). Thomson (1982), provides a nonparametric approach to estimating mixed spectra, based on a multitapering.

A more general specification for periodic time series, including the possibility of strongly exogenous regression effects, is the following:

$$\begin{array}{rcl} y_t & = & \boldsymbol{\beta}'\mathbf{x}_t + u_t, \;\; t = 1, 2, \ldots, n, \\ u_t & = & \alpha_{0t} + \sum_{j=1}^{M} \Big(\alpha_{jt} \cos(\lambda_j t) + \alpha^*_{jt} \sin(\lambda_j t) \Big) + \varepsilon_t. \end{array} \tag{7}$$

The vector $\mathbf{x}_t$ contains the values of p exogenous regressors. The process α_{0t} is the *red noise* component of the series, capturing low frequency movements, formulated as

$$\alpha_{0t} = \phi \alpha_{0,t-1} + \eta_{0t}, \quad \eta_{0t} \sim \text{i.i.d. } \mathrm{N}(0, \sigma^2_{\eta 0}). \tag{8}$$

A fractional noise process (also known as *pink noise*) is a likely candidate for the low frequency variability of y_t. However, for the kind of climatological applications to be discussed later, and namely paleoclimate time series, the typical spectral shape suggests a bounded spectrum in the vicinity of the zero frequency. See Mann and Lees (1996) and Wunsch (2003), among others. The j-th component cycle, $\alpha_{jt} \cos(\lambda_j t) + \alpha^*_{jt} \sin(\lambda_j t)$, is a Gaussian fSW process with memory parameter d_j, frequency parameter λ_j, disturbance error variance $\sigma^2_{\eta j}$, and unconditional variance $\sigma^2_{\alpha j}$. Finally ε_t is a Gaussian white noise process, $\varepsilon_t \sim$ i.i.d. $\mathrm{N}(0, \sigma^2_\varepsilon)$.

The components are assumed to be mutually independent. Hence, conditional on $\mathbf{x}_t$, $\mathrm{E}(y_t|\mathbf{x}_t) = \boldsymbol{\beta}'\mathbf{x}_t$ and due to additivity and independence, the autocovariance function of y_t, $\gamma(k) = \mathrm{Cov}(y_t, y_{t-k}|\mathbf{x}_t, \mathbf{x}_{t-k})$, is the sum of the autocovariance functions of the components,

$$\gamma(k) = \phi^k \frac{\sigma^2_{\eta 0}}{1 - \phi^2} + \sum_{j=1}^{M} \sigma^2_{\alpha_j} \frac{\Gamma(1 - d_j)\Gamma(d_j + k)}{\Gamma(1 - d_j + k)\Gamma(d_j)} \cos(\lambda_j k) + I(k = 0)\sigma^2_\varepsilon, \tag{9}$$

where $I(\cdot)$ is the indicator function, and spectral density

$$f(\omega) = \frac{1}{2\pi} \left\{ \frac{\sigma^2_{\eta 0}}{1 + \phi^2 - 2\phi \cos(\omega)} + \sum_{j=1}^{M} \sigma^2_{\eta j} \left\{ \left| 2 \sin\left(\frac{\omega - \lambda_j}{2} \right) \right|^{-2d_j} + \left| 2 \sin\left(\frac{\omega + \lambda_j}{2} \right) \right|^{-2d_j} \right\} + \sigma^2_\varepsilon \right\}.$$

5 Inference

Due to the availability of closed form expressions for the autocovariance and spectral density functions, the parameters of model (7) can be estimated either in the time domain or in the frequency domain. In the former case, under the Gaussian assumption, the likelihood can be evaluated exactly with the support of the Durbin-Levinson (DL) algorithm

(Levinson, 1946; Durbin, 1960). In the latter, we use the Whittle likelihood approximation (Whittle, 1953). The estimation of the components of variability in (7), conditional on the parameter estimates, again uses the DL factorization of the inverse autocovariance matrix.

5.1 Profile and residual maximum likelihood estimation

Let $\mathbf{y} = [y_1, y_2, \ldots, y_n]'$ denote the stack of the time series observations. The linear model (7) implies the representation $\mathbf{y} = \mathbf{X}\boldsymbol{\beta} + \mathbf{u}$, with $\mathbf{X} = [\mathbf{x}_1', \mathbf{x}_2', \ldots, \mathbf{x}_n']'$ and $\mathbf{u} = [u_1, u_2, \ldots, u_n]'$, so that $\mathbf{u} \sim \mathrm{N}(\mathbf{0}, \boldsymbol{\Gamma}_n)$, where $\boldsymbol{\Gamma}_n$ is the Toeplitz matrix

$$\boldsymbol{\Gamma}_n = \begin{bmatrix} \gamma(0) & \gamma(1) & \cdots & \cdots & \gamma(n-1) \\ \gamma(1) & \gamma(0) & \ddots & \ddots & \gamma(n-2) \\ \vdots & \ddots & \ddots & \ddots & \vdots \\ \gamma(n-2) & \ddots & \ddots & \ddots & \gamma(1) \\ \gamma(n-1) & \gamma(n-2) & \cdots & \gamma(1) & \gamma(0) \end{bmatrix},$$

with elements given by (9).

Letting $\boldsymbol{\theta}_j = (d_j, \lambda_j, \sigma^2_{\eta_j})'$, $j = 1, \ldots, M$, and $\boldsymbol{\theta}_0 = (\phi, \sigma^2_{\eta_0})'$, $\boldsymbol{\Gamma}_n$ depends on the vector of unknown parameters $\boldsymbol{\theta} = (\boldsymbol{\theta}_0', \boldsymbol{\theta}_1', \ldots, \boldsymbol{\theta}_m', \sigma^2_\varepsilon)'$.

The Gaussian log-likelihood is

$$\ell(\boldsymbol{\theta}, \boldsymbol{\beta}; \mathbf{y}) = -\frac{n}{2}\log(2\pi) - \frac{1}{2}\log|\boldsymbol{\Gamma}_n| - \frac{1}{2}(\mathbf{y} - \mathbf{X}\boldsymbol{\beta})'\boldsymbol{\Gamma}_n^{-1}(\mathbf{y} - \mathbf{X}\boldsymbol{\beta})$$

Maximising with respect to $\boldsymbol{\beta}$ yields the generalized least squares estimator

$$\tilde{\boldsymbol{\beta}} = (\mathbf{X}'\boldsymbol{\Gamma}_n^{-1}\mathbf{X})^{-1}\mathbf{X}'\boldsymbol{\Gamma}_n^{-1}\mathbf{y}.$$

Replacing into the previous expression gives the profile likelihood

$$\ell_\beta(\theta; \mathbf{y}) = -\frac{n}{2}\log(2\pi) - \frac{1}{2}\log|\boldsymbol{\Gamma}_n| - \frac{1}{2}\mathbf{y}'\mathbf{P}\mathbf{y},$$

with $\mathbf{P} = \boldsymbol{\Gamma}_n^{-1} - \boldsymbol{\Gamma}_n^{-1}\mathbf{X}(\mathbf{X}'\boldsymbol{\Gamma}_n^{-1}\mathbf{X})^{-1}\mathbf{X}'\boldsymbol{\Gamma}_n^{-1}$.

The marginal likelihood of the $n-p$ linear transformation of the data, $\mathbf{y}^* = \mathbf{A}'\mathbf{y}$, which is invariant to $\boldsymbol{\beta}$, where $\mathbf{A}$ is an $(n-k) \times n$ matrix spanning the null space of $\mathbf{X}$, i.e., it is chosen so that $\mathbf{A}(\mathbf{A}'\mathbf{A})^{-1}\mathbf{A}' = \mathbf{I} - \mathbf{X}(\mathbf{X}'\mathbf{X})^{-1}\mathbf{X}'$,

$$\ell(\theta; \mathbf{y}^*) = -\frac{n-p}{2}\log(2\pi) - \frac{1}{2}\log|\boldsymbol{\Gamma}_n| - \frac{1}{2}\mathbf{y}'\mathbf{P}\mathbf{y} - \frac{1}{2}|\mathbf{X}'\boldsymbol{\Gamma}_n^{-1}\mathbf{X}|,$$

The value $\tilde{\boldsymbol{\theta}}$ maximizing is known in the literature as a restricted maximum likelihood (REML) estimator. See Verbyla (1990) and Smyth and Verbyla (1996). See also Doornik and Ooms (2003) for the discussion of the merits of various likelihoods for the estimation of ARFIMA models.

The evaluation of the log-likelihood entails the inversion and the determinant of a possibly large dimensional covariance matrix. The Durbin–Levinson algorithm, see Brockwell and Davis (1991), performs the factorization (Pourahmadi, 2001, chapter 7):

$$\boldsymbol{\Gamma}_n^{-1} = \boldsymbol{\Phi}_n' \mathbf{D}_n \boldsymbol{\Phi}_n,$$

where $\mathbf{D}_n = \operatorname{diag}\left(v_0^{-1}, v_1^{-1}, \ldots, v_{n-1}^{-1}\right)$, $v_k = \operatorname{Var}(u_t | u_{t-1}, \ldots, u_{t-k})$, i.e., the conditional variance of $u_t = y_t - \boldsymbol{\beta}' \mathbf{x}_t$, given k past values, and

$$\boldsymbol{\Phi}_n = \begin{bmatrix} 1 & 0 & 0 & \cdots & 0 \\ -\phi_{11} & 1 & 0 & \cdots & 0 \\ -\phi_{22} & -\phi_{21} & 1 & \cdots & 0 \\ \vdots & \vdots & \cdots & \ddots & \vdots \\ -\phi_{n-1,n-1} & -\phi_{n-1,n-2} & -\phi_{n-1,n-3} & \cdots & 1 \end{bmatrix}.$$

Appendix A deals with the maximum likelihood estimation in the case when the fSW process collapses to a deterministic cycle with discrete spectrum.

5.2 Whittle likelihood estimation

The Whittle likelihood is based on the asymptotic approximation (Brockwell and Davis, 1991, section 4.5.2)

$$\boldsymbol{\Gamma}_n^{-1} \approx \frac{1}{2\pi} \mathbf{W}_n \mathbf{F}_n^{-1} \mathbf{W}_n^H,$$

where $\mathbf{W}_n$ is the $n \times n$ Fourier matrix

$$\mathbf{W}_n = \left\{ \frac{1}{\sqrt{2\pi n}} e^{\imath \omega_j t}, t = 1, \ldots, n; j = 0, \ldots, n-1 \right\},$$

$\mathbf{F}_n = \operatorname{diag}\{f(\omega_0, f(\omega_1), \ldots, f(\omega_{n-1})\}$, and $\mathbf{W}_n^H$ is the complex conjugate transpose of $\mathbf{W}_n$, such that $\mathbf{W}_n \mathbf{W}_h^H = (2\pi)^{-1} \mathbf{I}$.

Denoting the Fourier tranform of y_t and $\mathbf{x}_t$ by

$$J_y(\omega_j) = \frac{1}{\sqrt{2\pi n}} \sum_{t=1}^{n} y_t e^{-\imath \omega_j t}, \mathbf{J}_x(\omega_j) = \frac{1}{\sqrt{2\pi n}} \sum_{t=1}^{n} \mathbf{x}_t e^{-\imath \omega_j t},$$

where $\omega_j = 2\pi j/n$, $j = 0, 1, \ldots, n-1$, are the Fourier frequencies, and letting $\mathbf{W}_n^H \mathbf{y} = \mathbf{J}_y$, $\mathbf{J}_y = (J_y(\omega_0), J_y(\omega_1), \ldots, J_y(\omega_{n-1}))'$, $\mathbf{W}_n^H \mathbf{X} = \mathbf{J}_x$, $\mathbf{J}_x$ being the $n \times p$ matrix with element in position (j, k) given by $\frac{1}{\sqrt{2\pi n}} \sum_{t=1}^{n} x_{kt} e^{-\imath \omega_j t}$, the maximum likelihood estimator of $\boldsymbol{\beta}$ is

$$\tilde{\boldsymbol{\beta}} = (\mathbf{J}_x^H \mathbf{F}_n^{-1} \mathbf{J}_x)^{-1} \mathbf{J}_x^H \mathbf{F}_n^{-1} \mathbf{J}_y,$$

and the profile Whittle likelihood is

$$\ell_W(\boldsymbol{\theta}; \mathbf{y}) = -\frac{n}{2} \log(2\pi) - \frac{1}{2} \sum_{j=0}^{n-1} \left\{ \log f(\omega_j) + \frac{I_{\hat{u}}(\omega_j)}{f(\omega_j)} \right\},$$

where $I_{\hat{u}}(\omega_j) = |J_y(\omega_j) - \mathbf{J}_(\omega_j)\tilde{\boldsymbol{\beta}}|^2$ is the periodogram of $\hat{u}_t = y_t - \mathbf{x}_t'\tilde{\boldsymbol{\beta}}$.

The asymptotic properties of the maximum likelihood estimator of $\boldsymbol{\theta}$ have been dealt with by Hosoya (1997), assuming the cycle frequencies are known; Giraitis et al. (2001) consider the estimation in the case of unknown λ_j.

While in our specific applications λ_j can be considered as given, as they represent seasonal frequencies of a subannual time series or because they are given by orbital theory, the regularity conditions under which the MLE's are consistent asymptotically normal are violated in the deterministic case, when $d_j \to 1/2$ and $\sigma^2_{\eta j} \to 0$, for some j. A deterministic cycle can be however estimated by including the term $\alpha\cos(\lambda_j t)+\alpha^*\sin(\lambda_j t)$ in the regression component, and the consistency of the MLE of $(\alpha, \alpha^*, \lambda_j)$ follows from Hannan (1973). For the estimation of frequency of a deterministic cycle, see Quinn (2012).

5.3 Signal Extraction and Prediction

Consider the problem of estimating the signal $\mathbf{s} = (s_1, \ldots, s_t, \ldots, s_{n+h})', h \geq 0$, where, e.g., $s_t = \alpha_{kt}\cos(\lambda_k t) + \alpha^*_{kt}\sin(\lambda_k t)$, for a given k, conditional on $\tilde{\boldsymbol{\theta}}$ and $(\mathbf{y}, \mathbf{X})$.

The optimal estimator is

$$\hat{\mathbf{s}} = \boldsymbol{\Gamma}_{s,y}\tilde{\boldsymbol{\Phi}}_n'\tilde{\mathbf{D}}_n\tilde{\boldsymbol{\Phi}}_n(\mathbf{y} - \mathbf{X}\tilde{\boldsymbol{\beta}})$$

where $\boldsymbol{\Gamma}_{s,y} = \mathrm{Cov}(\mathbf{s}, \mathbf{y})$ has (i, j) element

$$\tilde{\sigma}^2_{\eta k}\frac{\Gamma(1-2\tilde{d}_k)\Gamma(\tilde{d}_k + |i-j|)}{\Gamma(1-\tilde{d}_k+|i-j|)\Gamma(\tilde{d}_k)\Gamma(1-\tilde{d}_k)}\cos(\tilde{\lambda}_k(|i-j|)).$$

The minimum mean square estimator of the other components and the prediction of y_t follows straightforwardly.

6 Mauna Loa Atmospheric CO_2 Data

The series considered in this illustration consists of monthly atmospheric carbon dioxide measurements collected at the summit of Mauna Loa mountain (Hawaii), dealing with concentrations in parts per million (ppm), over the period January 1958 - June 2020 (Source: National Oceanographic and Atmospheric Administration Climate Monitoring and Diagnostics Laboratory, and Keeling et al. (1976)).

The series is very relevant for climate change discussion, being the longest instrumental record available of atmospheric CO_2; it is also a testbed for the class of k-factor generalized Gegenbauer processes, see Woodward et al. (1998) and McElroy and Holan (2012, 2016), which have been fitted to the second differences of the series.

While its distinctive upward pattern is attributed to anthropogenic causes (combustion of fossil fuels and long-term changes in land use), the series displays important inter-annual and intra-annual movements.

Seasonality is indeed prominent, and the changes in the amplitude and phase of the annual cycle have been the subject of a rich debate. The seasonal cycle, which peaks in May and has a trough in October, is driven by the metabolic activity of terrestrial plants

and soils: the process of carbon uptake and release of the land biosphere is such that CO_2 concentrations increase in winter, when plant respiration dominates, and decreases in summer, when the photosyntesis uptake dominates.

A significant amplitude increase was documented already by Bacastow et al. (1985), while Keeling et al. (1996) also detected a change in the phase, implying an advance of the seasonal cycle of about 7 days. These references attributed the changes to global warming and longer growing seasons. Singular spectrum analysis of the Mauna Loa time series (Dettinger and Ghil, 1998) provided further support for the changes in the seasonal cycle. Kaufmann (2007) identifies statistically significant variation in the anomalies pertaining to the monthly concentrations of April and October.

Amplitude trends and phase changes reflect changes in the global carbon cycle and its response to climate change; thus, their attribution is an important matter of investigation, see Forkel et al. (2016), Bastos et al. (2019) and Wang et al. (2020), for some recent contribution and discussion.

The interannual variation of CO_2 concentrations has been related to the El Niño Southern Oscillation (ENSO) phenomenon already by Bacastow (1976), who identified the component by a semiparametric detrending and seasonal adjustment method, and used the Southern Oscillation Index (SOI) as a measure of ENSO. The correlation has been confirmed by alternative methods (Dettinger and Ghil, 1998) and measurements (Chatterjee et al. (2017). As highlighted by Zeng et al. (2005), the strong correlation between the interannual variation and the SOI index is quite remarkable, considering the chain of causal links that relates the two phenomena. ENSO originates in the tropical Pacific Ocean, but is one of the main drivers of interannual global climate variability. Volcanic eruptions also contribute to interannual variation of CO_2. Hendry and Pretis (2013) conclude, however, that natural factors are not sufficient to explain the changes in CO_2 concentrations. They identify significant anthropogenic contributions using an autoregressive distributed lag model selected by a general to specific modelling approach.

Denoting by y_t the Mauna Loa CO_2 monthly time series, we formulate and estimate the following specification:

$$y_t = \beta_0 + \beta_1 t + \beta_2 t^2 + \alpha_{0t} + \sum_{j=1}^{5} \left(\alpha_{jt} \cos(\lambda_j t) + \alpha^*_{jt} \sin(\lambda_j t) \right) + \alpha_{6t} \cos(\pi t).$$

The regression component features a quadratic trend, α_{0t} is the AR(1) red noise process (8), modelling the low-frequency variability of CO_2 concentrations, and the seasonal component is modelled by the six fSW cycles defined at the seasonal frequencies $\lambda_j = \frac{\pi}{6} j, j = 1, \ldots, 6$.

When the model is estimated in the time domain by maximum likelihood, the regression coefficients are significant and the MLE of ϕ is 0.9998, so that the red noise process actually turns *brown*, and $\tilde{\sigma}^2_{\eta 0} = 0.0212$. As for the fSW seasonal cycles, the estimates presented in table 1 point out that the cycles at the harmonics $\pi/2$ (3 cycles per year), and $2\pi/3$ (4 cycles per year) are deterministic, contributing with a line or narrow band component to the spectrum, whereas the cycle at the π frequency (six cycles per year) is not present.

j	λ_j	$\tilde{d}_j$	$\tilde{\sigma}^2_{\eta j}$	$\tilde{\sigma}^2_{\alpha j}$
1	$\pi/6$	0.4995	0.0127	4.0165
2	$\pi/3$	0.4980	0.0041	0.3297
3	$\pi/2$	0.5000	0.0000	0.0032
4	$2\pi/3$	0.5000	0.0000	0.0027
5	$5\pi/6$	0.0569	0.0241	0.0243
6	π	0.5000	0.0000	0.0000

Table 1: Maximum likelihood estimates of the fSW cycle memory and variance parameters.

The broad band components are identified at the fundamental frequency (1 cycle per year), and at $\pi/3$, the semiannual frequency. The seasonal cycle at $5\pi/6$ (2.4 cycles per year) is also estimated as a broadband component, although it shows little persistence and variability.

The model provides a good fit: the estimated prediction error variance is $\tilde{v}_{n-1} = 0.0913$, which represent 6.04% of the variance of Δy_t. The standardized residuals show no significant autocorrelation, the sample autocorrelations at lags 1 and 12 resulting 0.0052 and 0.0199, respectively, and those of their squares being equal to 0.0120 and 0.0775, respectively; the Jarque-Bera test statistic resulted 4.6479.

The estimated components provide useful insight. Figure 2 displays the trend estimate, resulting as $\tilde{\mu}_t = \sum_{j=0}^{2} \tilde{\beta}_j t^j + \tilde{\alpha}_{0t}$, where $\tilde{\alpha}_{0t}$ is obtained according to 5.3, as the minimum mean square estimate of the red (possibly brown) noise component, and is displayed in the bottom panel of the figure.

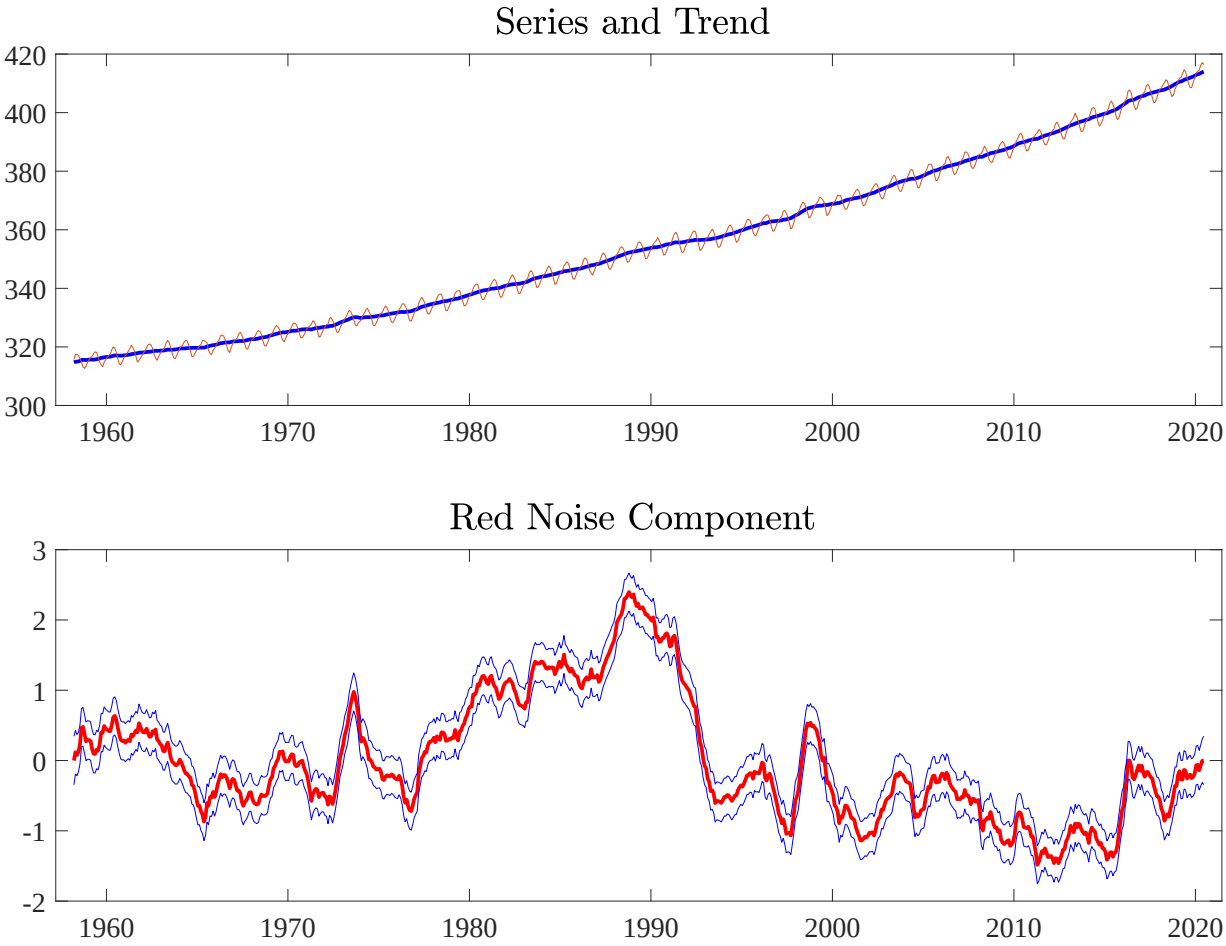

Figure 2: Minimum mean square estimates of the trend component, $\tilde{\mu}_t = \sum_{j=0}^{2} \tilde{\beta}_j t^j + \tilde{\alpha}_{0t}$. The bottom panel displays the minimum mean square estimates of the red, or brown, possibly, component $\tilde{\alpha}_{0t}$.

The literature referenced above has identified the interannual variability as the change in low frequency component of CO_2 concentrations, which is extracted by various parametric and nonparametric methods both in the time and frequency domains. In our setup it is quite natural to identify it as $\Delta\alpha_{0t}$. To investigate its relation with the ENSO phenomenon, figure 3 plots on a standardized scale the Southern Oscillation Index (SOI) time series along with $\Delta\tilde{\alpha}_{0t}$. The SOI measures the normalized surface pressure difference between Tahiti and Darwin (Australia), and is an expression of the ENSO, which takes negative values during El Niño episodes and positive values during La Niña episodes.

The picture reveals a negative association between the two series, which is also confirmed by the plot of the cross-correlations in the bottom panel of the figure, whose pattern confirms that SOI leads the the interannual variation in CO_2 by 3-5 months. The literature reports a maximum absolute correlation of 0.5, but this is computed on the smoothed SOI and CO_2 growth. Indeed, it could be argued that the correlation is inflated by the fact that the estimates of $\Delta\alpha_{0t}$ are conditional on the full available sample. To address this point we also present the cross-correlation function of the SOI and the real time estimates of the interannual variation in CO_2, which are lower, yet significant. The real time estimate of the changes of the red noise component is obtained by projecting $\Delta\alpha_{0t}$ on $(\Delta y_2, \ldots, \Delta y_t)'$.

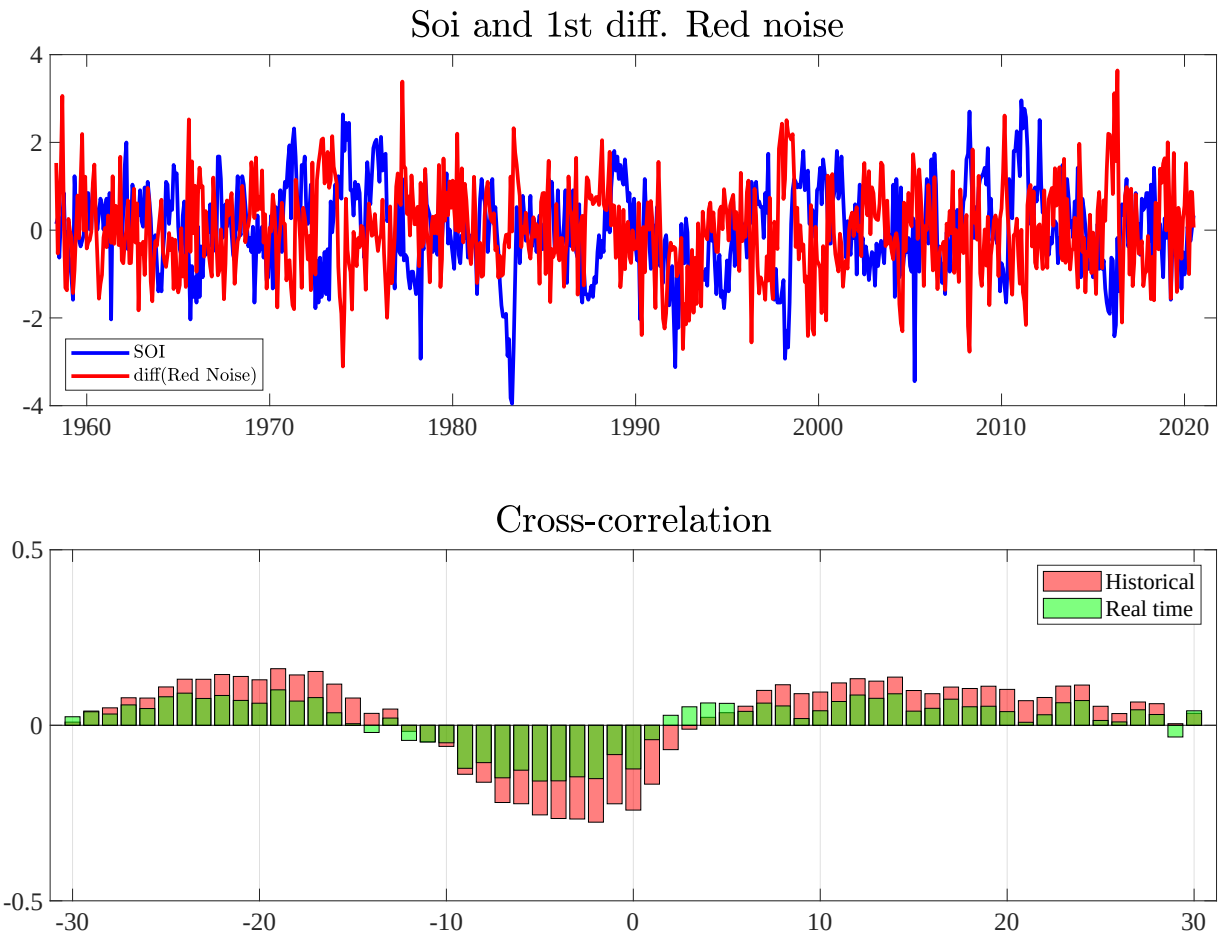

Figure 3: SOI index and first differences of the Red Noise component (standardized scale). The bottom plot is the sample cross-correlation between the SOI index and the first differences of the red noise component, estimated both conditioning on the full available series and in real time.

The minimum mean square estimates of the fSW cycles at the annual frequency, $\tilde{\alpha}_{1t}\cos(\pi t/6) + \tilde{\alpha}^*_{1t}\sin(\pi t/6)$, $t = 1, \ldots, n$, and at the semiannual (2 cycles per year) frequency, $\tilde{\alpha}_{2t}\cos(\pi t/3) + \tilde{\alpha}^*_{2t}\sin(\pi t/3)$, are plotted in the top panels of figure 4. As implied by the estimates of their variance (table 1) the annual component has the largest magnitude and the plot reveals that these components vary over time. The time-varying amplitude, $\tilde{A}_{jt} = \sqrt{\tilde{\alpha}^2_{jt} + \tilde{\alpha}^{2*}_{jt}}$, and phase $\tilde{\varphi}_{jt} = \arctan(\tilde{\alpha}^{2*}_{jt}/\tilde{\alpha}^2_{jt}), j = 1, 2$, of the two fSW components are displayed in the bottom panels of figure 4.

The overall change in amplitude during the period considered amounts to 0.5 ppm for the fundamental cycle and to 0.2 ppm for the semiannual one. The changes imply that CO_2 release in winter months has relatively increased and uptake in summer months has declined. The estimated percent change in amplitude per year of the seasonal component, resulting from the sum of the six cycles, is slightly above that reported by Graven et al. (2013) (0.36% versus 0.32%), which can be due to the faster amplitude increase of the most recent years. The trend in the amplitude shows a deceleration after the 1980s, consistent with Wang et al. (2020), but it is subject to a more rapid increase in the recent years. As mentioned above, the attribution of the amplitude increase is controversial. Forkel et al. (2016) relate it to the stimulation of photosynthesis and vegetation growth induced by climate change.

A relevant phase change is also evident from figure 4. Our estimates imply a phase advance of 20 days for the fundamental cycle, resulting from $30.44\frac{6}{\pi}(\hat{\varphi}_n - \hat{\varphi})_1)$, where 30.44 is the average month length. The semiannual cycle is also subject to a phase advance, but of only 6 days. The combined effects imply that the May annual peak becomes more prominent with time, while September emerges as the seasonal trough.

7 Cycles and Variability in Paleoclimate Data

Figure 5 displays four paleoclimate time series dealing with ice cores reconstructions of temperatures, methane (CH_4), carbon dioxide (CO_2) concentrations and ice volume. The first three series are obtained by the European Project for Ice Core in Antartica (EPICA) (Jouzel et al., 2007; Loulergue et al., 2008; Lüthi et al., 2008), while the ice volume series is obtained from Lisiecki and Raymo (2005).

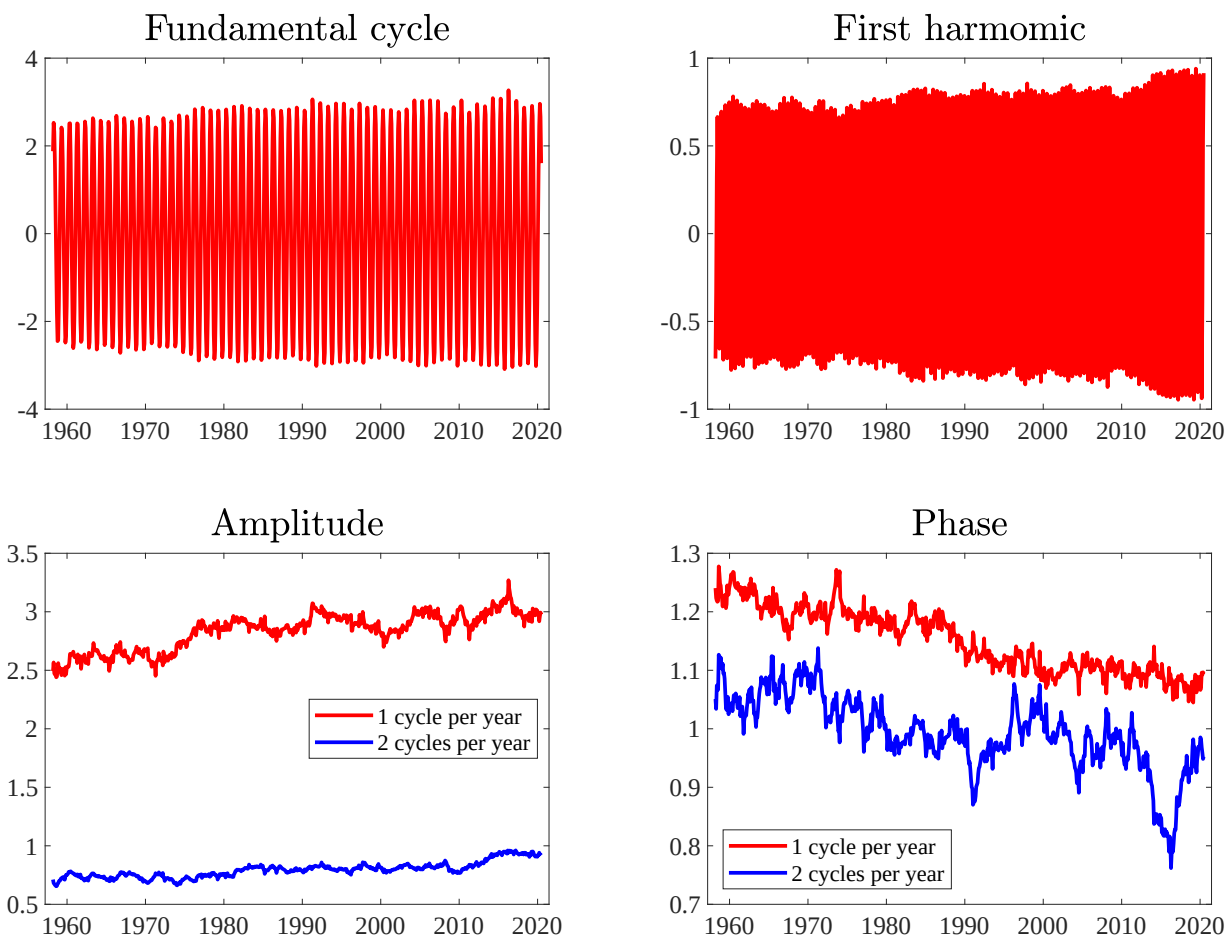

Figure 4: Minimum mean square estimates of the fSW cycles at the fundamental (annual) frequency, $\tilde{\alpha}_{1t}\cos(\pi t/6)+\tilde{\alpha}^*_{1t}\sin(\pi t/6)$ (top left) and at the semiannual (2 cycles per year) frequency, $\tilde{\alpha}_{2t}\cos(\pi t/3)+\tilde{\alpha}^*_{2t}\sin(\pi t/3)$ (top right). Amplitude, $\tilde{A}_{jt}=\sqrt{\tilde{\alpha}^2_{jt}+\tilde{\alpha}^{2*}_{jt}}, j=1,2,$ (bottom left), and phase $\tilde{\varphi}_{jt}=\arctan(\tilde{\alpha}^{2*}_{jt}/\tilde{\alpha}^2_{jt})$ (bottom right) of the two fSW components.

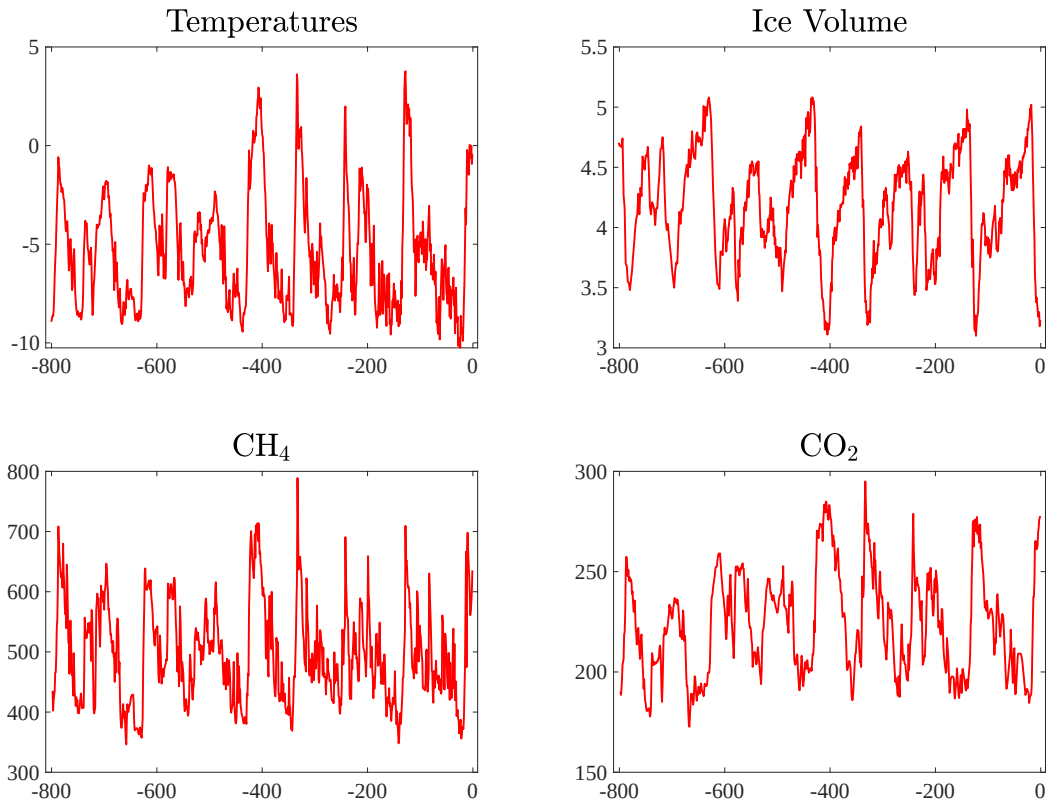

Figure 5: Paleoclimate time series extending back to 800 kyr: temperature, ice volume, and atmospheric concentrations of CH_4 and CO_2.

The series display substantial recurrent co-movements referred to as *glacial cycles*: during glaciations, temperature and trace gases concentrations stay below their mean for prolonged periods, while for ice volume the pattern is reversed. According to the paleoclimatic literature and the Milankovitch theory (Hays et al., 1976), glacial cycles are attributed to changes in Earth's orbital geometry over time, which affects incoming solar radiation. The three main sources of variation are: i. eccentricity of the Earth orbit round the Sun, due to gravitational effects of other planets in the solar system, which varies deterministically with a periodicity of about 100 kyr; ii. obliquity or tilt of the Earth's axis of rotation, which varies with a period of 41 kyr; iii. precession of the equinoxes. This component has periodicities of about 23 and 19 kyr.

The four series have been recently investigated by Davidson et al. (2016) and Castle and Hendry (2020, chapter 6). Davidson et al. (2016) conducted a variety of tests of unit root nonstationarity, and found evidence against it. They estimate a vector autoregressive (VAR) model with exogenous forcing of orbital variables and conclude that Milankovitch

theory predicts glacial cycles remarkably well, and that while temperatures Granger-cause greenhouse gas concentrations, the reverse hypothesis is not supported. Castle and Hendry (2020, chapter 6) model Ice volume, CO_2 and temperatures according to a VAR model with strongly exogenous orbital forcing variables. They find that, while the Milankovitch hypothesis cannot account for all aspects of glacial cycles, nonlinear feedbacks or interactions between the three orbital components have significant effects on paleoclimate time series, and find support for an endogenous response of CO_2 to orbital forcing.

Larger cointegrated VAR systems are adopted by Kaufmann and Juselius (2013, 2016) and Kaufmann and Pretis (2020, 2021). These extend the range of endogenous paleoclimate variables and estimate long-run cointegration relations between solar insolation and climate variables. These reference find support for a weak form of the Milankovitch theory in which solar insolation drives glacial cycles, with perturbations imposed by internal dynamics by which the climate system corrects the disequilibrium from the cointegrating relations.

A key issue deals with the role of the above three orbital components in explaining the variability in the climate and trace gases. It is evident from the plots that glacial cycles in the late Pleistocene occur at intervals of 100 kyr; however, eccentricity is the smallest of the orbital forcings, accounting for minor fluctuations in the amplitude of the insolation signal. This is known as the '100 kyr' problem. Hence, the detailed mechanism by which small changes in insolation become amplified to drive major climatic changes remains unclear. A nonlinear response of the climate system to relatively weak eccentricity variations has been advocated by Paillard (2001), see also Wunsch (2003) for the 'drunkard climb' hypothesis used to explain the saw tooth pattern of ice volume.

An important strand of the literature has aimed at quantifying the contribution of the orbital components via a decomposition of the total variability of paleoclimate series in the frequency domain. This entails estimation of a possibly mixed spectrum or pseudo-spectrum, for which purpose the use of Thomson (1982) multitaper spectral method, see also Percival and Walden (2020), is prominent. Given the deterministic nature of orbital forcing, the ability to distinguish narrow-band (discrete spectra) components from background broad-band components is quintessential to the identification of the components of paleoclimate variability. See Mitchell (1976), Mann and Lees (1996), Wunsch (2003) Meyers et al. (2008), Ditlevsen et al. (2020), among others.

Our contribution to this literature is to provide an alternative parametric approach, based on the additive model (7), to the quantification of the components of paleoclimate variability via the spectrum. We adopt the logarithmic transformation of the variables used by Davidson et al. (2016), namely $y_t = \log(x_t + 16)$ for temperatures, $y_t = -\log(8 - x_t)$ for ice, and $y_t = \log(x_t/100)$ for both CH_4 and CO_2, where x_t denotes the original measurement. The model features a constant, a red noise component, specified as in (8), and four fSW cycles associated to the orbital frequencies $\lambda_1 = \pi/50$ (eccentricity), $\lambda_2 = 2\pi/41$ (obliquity), $\lambda_3 = 2\pi/23$ and $\lambda_4 = 2\pi/19$ (precession):

$$y_t = \beta_0 + \alpha_{0t} + \sum_{j=1}^{4} \left(\alpha_{jt} \cos(\lambda_j t) + \alpha^*_{jt} \cos(\lambda_j t) \right). \tag{10}$$

The red noise captures the internal stochastic variability of the climate system, see Mitchell (1976), while the fSW cycles aim at capturing the variability due to climate response to orbital forcing.

The maximum likelihood estimates of the parameters are presented in table 2. The estimated autoregressive parameter of the red noise component is positive and high, but less than 1 for all series. The fSW cycles associated to eccentricity and obliquity are estimated to be deterministic for all series. The only orbital component characterized by a broad-band spectrum is the 23 kyr cycle (precession), whereas the 19 kyr cycle makes a negligible contribution. The presence of narrow spectral peaks is consistent with Muller and MacDonald (1997).

	Parameter estimates			
	Temp.	Ice v.	CH_4	CO_2
$\tilde{\beta}_0$	2.3317	-1.3331	1.5886	0.7967
$\tilde{\phi}$	0.9240	0.9638	0.8705	0.9669
$\tilde{\sigma}^2_{\eta 0}$	0.0057	0.0005	0.0039	0.0006
$\tilde{d}_1$	0.5000	0.5000	0.5000	0.5000
$\tilde{\sigma}^2_{\eta 1}$	0.0000	0.0000	0.0000	0.0000
$\tilde{d}_2$	0.5000	0.5000	0.5000	0.5000
$\tilde{\sigma}^2_{\eta 2}$	0.0000	0.0000	0.0000	0.0000
$\tilde{d}_3$	0.4695	0.4832	0.4467	0.5000
$\tilde{\sigma}^2_{\eta 3}$	0.0006	0.0001	0.0002	0.0000
$\tilde{d}_4$	0.3753	0.5000	0.5000	0.5000
$\tilde{\sigma}^2_{\eta 4}$	0.0000	0.0000	0.0000	0.0000

	Diagnostics			
	Temp.	Ice v.	CH_4	CO_2
p.e.v.	0.0065	0.0006	0.0042	0.0006
R^2	0.9075	0.9583	0.8388	0.9559
$r(1)$	0.0382	0.0352	0.0323	0.3493
$r(2\|1)$	-0.0537	0.0849	-0.0081	-0.1128
$r_{sq}(1)$	0.1591	0.1811	0.1640	0.2918
Skewness	-0.2548	-0.3451	0.8904	0.5768
Kurtosis	4.3064	4.3159	6.6686	4.8094

Table 2: Maximum likelihood estimates of the parameters of model (10) and model diagnostics: prediction error variance (p.e.v.), coefficient of determination, R^2; $r(1)$ is the first order sample residual autocorrelation; $r(2|1)$ is the residuals sample partial autocorrelation at lag 2; $r_2(1)$ is the first order autocorrelation of the squares of the residuals; the last two rows are the standardized third and fourth moments of the residuals.

Model (10) proves quite effective in capturing the dynamic structure of the series. The prediction error variance, estimated by $\tilde{v}_{n-1}$, is reported in table 2, along with the coefficient of determination, $R^2 = 1 - \frac{\tilde{v}_{n-1}}{\tilde{v}_0}$. Diagnostic checking is carried out on the

standardized residuals $\mathbf{e} = \tilde{\mathbf{D}}_n^{1/2}\tilde{\mathbf{\Phi}}_n(\mathbf{y} - \mathbf{X}\tilde{\boldsymbol{\beta}})$: their autocorrelation at lag one, reported in table 2 as $r(1)$, and the partial autocorrelation at lag two, $r(2|1)$, show that no residual serial dependence is present, with the exception of CO_2. A possible cause is a change in level around $t = -600$. The positive autocorrelation of the squared standardized residuals at lag one, $r_{sq}(1)$, suggests that some unaccounted conditional heteroscedasticity is present. Also, the skewness and kurtosis of the sampling distribution of the residuals is somewhat at odds with the assumption of normality.

Figure 6 displays the minimum mean square estimates (MMSEs) of the red noise component for the temperature series (top panel). The dotted series in the background is the original demeaned series. The orbital component, resulting from $\sum_{j=1}^{4}\Big(\tilde{\alpha}_{jt}\cos(\lambda_j t) + \tilde{\alpha}^*_{jt}\cos(\lambda_j t)\Big)$, is plotted in the central panel, and the bottom plot are the MMSEs of the precession component, $\sum_{j=3}^{4}\Big(\tilde{\alpha}_{jt}\cos(\lambda_j t) + \tilde{\alpha}^*_{jt}\cos(\lambda_j t)\Big)$. It is evident that the cyclical movements attributed to precession are a minor component of the variation of temperatures. Similar considerations hold for the other series: figure 7 displays the MMSEs of the components the transformed ice volume series.

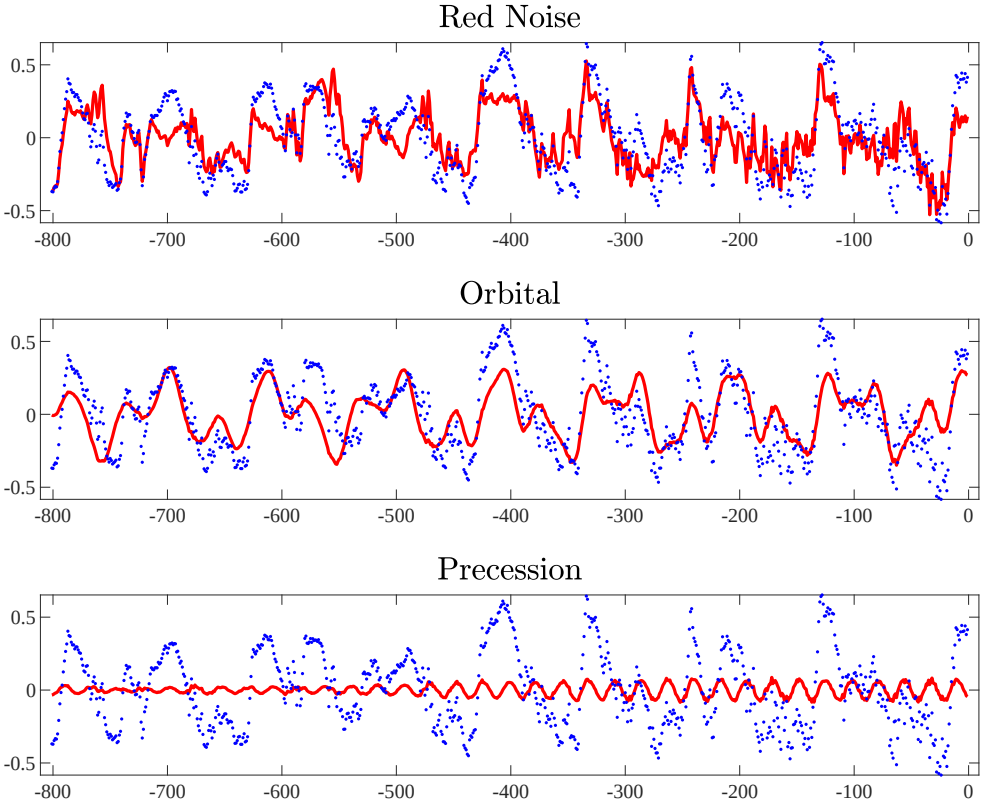

Figure 6: Temperature series. Minimum mean square estimates of the red noise component, the orbital component, $\sum_{j=1}^{4}\left(\tilde{\alpha}_{jt}\cos(\lambda_j t)+\tilde{\alpha}^{*}_{jt}\cos(\lambda_j t)\right)$, and the precession component, $\sum_{j=3}^{4}\left(\tilde{\alpha}_{jt}\cos(\lambda_j t)+\tilde{\alpha}^{*}_{jt}\cos(\lambda_j t)\right)$. The dotted series in the background is the original demeaned series.

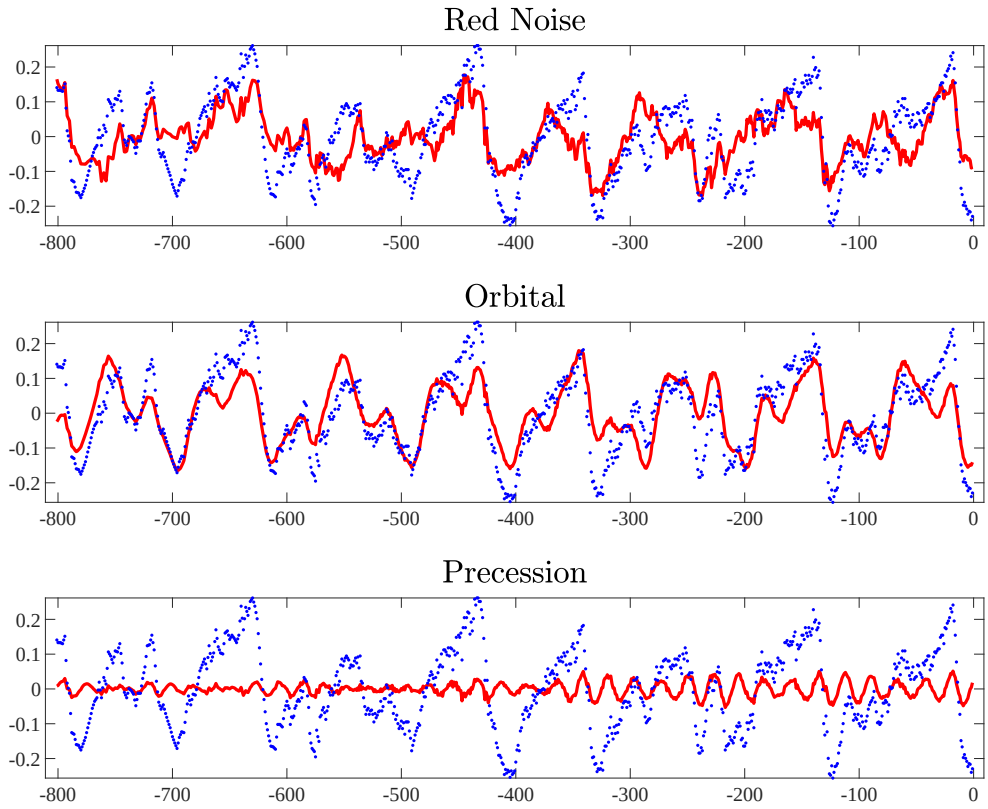

Figure 7: Ice volume series. Minimum mean square estimates of the red noise component, the orbital component, $\sum_{j=1}^{4}\left(\tilde{\alpha}_{jt}\cos(\lambda_j t)+\tilde{\alpha}^*_{jt}\cos(\lambda_j t)\right)$, and the precession component, $\sum_{j=3}^{4}\left(\tilde{\alpha}_{jt}\cos(\lambda_j t)+\tilde{\alpha}^*_{jt}\cos(\lambda_j t)\right)$. The dotted series in the background is the original demeaned series.

Our measurement model allows the quantification of the contribution of the components to the overall variability, since the following variance decomposition holds: $\text{Var}(y_t) = \sum_{j=0}^{4}\sigma^2_{\alpha j}$. When the model is estimated by maximum likelihood, the sample counterpart is the additive decomposition $\tilde{v}_0 = \sum_{j=0}^{4}\tilde{\sigma}_{\alpha j}$. Table 3 present the contribution of the red noise component ($\tilde{\sigma}^2_{\alpha 0}$), that of eccentricity ($\tilde{\sigma}^2_{\alpha 1}$), obliquity ($\tilde{\sigma}^2_{\alpha 2}$) and precession ($\tilde{\sigma}^2_{\alpha 3}+\tilde{\sigma}^2_{\alpha 4}$) to the total variability for the four series. The lower and upper confidence limits are obtained by generating 500 bootstrap samples according to the parametric bootstrap method presented in Appendix B. The red noise component accounts for 55.60%, 43.54%, 61.30% and 67.39% of the variance, respectively for temperatures, ice, CH_4 and CO_2. Hence, it represents the predominant source of variability for all series, excluding ice. These es-

timates are somewhat above the corresponding estimates for temperature proxy records from the Vostok ice cores obtained by Meyers et al. (2008). To explain the difference we notice that we estimate the spectrum of eccentricity and obliquity as a line spectrum, whereas Meyers et al. (2008) integrate the multitaper spectral density estimate across a neighbourhood of frequencies around the 100 and 41 kyr frequencies.

Table 3: Variance decompositions: contribution of the Red Noise and the three orbital cycles to the total variability of the series. The upper and lower 95% confidence limits are obtained by the parametric bootstrap discussed in Appendix B.

	Temperatures		
	Point est.	Lower Conf. Limit	Upper Conf. Limit
Red Noise	0.0392	0.0275	0.0536
Eccentricity	0.0170	0.0001	0.0529
Obliquity	0.0111	0.0000	0.0370
Precession	0.0032	0.0001	0.0080
Total Variance	0.0705	0.0407	0.1084

	Ice Volume		
	Point est.	Lower Conf. Limit	Upper Conf. Limit
Red Noise	0.0064	0.0040	0.0096
Eccentricity	0.0047	0.0001	0.0162
Obliquity	0.0024	0.0001	0.0070
Precession	0.0011	0.0002	0.0030
Total Variance	0.0147	0.0073	0.0271

	CH_4		
	Point est.	Lower Conf. Limit	Upper Conf. Limit
Red Noise	0.0160	0.0119	0.0207
Eccentricity	0.0064	0.0001	0.0196
Obliquity	0.0027	0.0000	0.0089
Precession	0.0010	0.0000	0.0029
Total Variance	0.0261	0.0159	0.0416

	CO_2		
	Point est.	Lower Conf. Limit	Upper Conf. Limit
Red Noise	0.0093	0.0056	0.0142
Eccentricity	0.0038	0.0001	0.0116
Obliquity	0.0006	0.0000	0.0019
Precession	0.0001	0.0000	0.0004
Total Variance	0.0138	0.0072	0.0219

Our estimates are more in line with Wunsch (2003), who questions the notion that paleoclimate variability is predominantly associated with the frequency bands attributed to

solar insolation. However, this is not quite the end of the story, as the red noise could may also result from the climate response to orbital forcing: the path from the orbital signal to climate and trace gases proxy records goes through several steps, outlined in Meyers et al. (2008), and possibly nonlinear and persistent transfer functions can be responsible for the dominance of the stochastic red noise component. A model of low frequency variation featuring hysteresis, such as $\alpha_{0t} = \phi\alpha_{0,t-1} + \alpha_{1t}\cos(\lambda_1 t) + \alpha^*_{1t}\sin(\lambda_1 t) + \eta_{0t}$, cannot be ruled out. When this specification is entertained on the four series, estimation becomes very unreliable, convergence being dramatically slow, although the likelihood is increased significantly.

8 Conclusions

The paper has proposed a novel time series model for persistent cycles, the fractional sinusoidal waveform (fSW) process. The model features stationary cyclical long memory and collapses to a line spectrum component when the parameters are on the boundary of their admissible range. Hence, it is suitable to analyze time series with mixed spectra. Likelihood inference and optimal signal extraction were discussed with reference to an additive model combining a broadband continuum component of variability with a number of fSW process.

The application to carbon dioxide concentration and paleoclimate time series have illustrated that the model can address some important questions raised with respect to the quantification of feature changes and the contribution to the total variability of deterministic forcing due to solar radiation.

References

Abadir, K., and Talmain, G. (2002). Aggregation, persistence and volatility in a macro model. *The Review of Economic Studies*, *69*(4), 749–779.

Andel, J. (1986). Long memory time series models. *Kybernetika*, *22*(2), 105–123.

Arteche, J., and Robinson, P. M. (2000). Semiparametric inference in seasonal and cyclical long memory processes. *Journal of Time Series Analysis*, *21*(1), 1-25.

Bacastow, R. (1976). Modulation of atmospheric carbon dioxide by the Southern Oscillation. *Nature*, *261*(5556), 116–118.

Bacastow, R., Keeling, C., and Whorf, T. (1985). Seasonal amplitude increase in atmospheric CO2 concentration at Mauna Loa, Hawaii, 1959–1982. *Journal of Geophysical Research: Atmospheres*, *90*(D6), 10529–10540.

Bastos, A., Ciais, P., Chevallier, F., Rödenbeck, C., Ballantyne, A. P., Maignan, F., ... others (2019). Contrasting effects of CO2 fertilization, land-use change and warming on seasonal amplitude of Northern Hemisphere CO2 exchange. *Atmospheric chemistry and physics*, *19*(19), 12361–12375.

Beran, J., Feng, Y., Ghosh, S., and Kulik, R. (2016). *Long-memory processes.* Springer.

Bisaglia, L., Bordignon, S., and Lisi, F. (2003). k-factor GARMA models for intraday volatility forecasting. *Applied Economics Letters*, *10*(4), 251–254.

Bordignon, S., Caporin, M., and Lisi, F. (2007). Generalised long-memory GARCH models for intra-daily volatility. *Computational Statistics & Data Analysis*, *51*(12), 5900–5912.

Brockwell, P. J., and Davis, R. A. (1991). *Time series: theory and methods: theory and methods*. Springer Science & Business Media.

Castle, J., and Hendry, D. F. (2020). Climate econometrics: An overview. In *Foundations and trends®in econometrics* (Vol. 10, p. 145-322). Now, the Essence of Knowledge. Boston-Delft.

Chatterjee, A., Gierach, M., Sutton, A., Feely, R., Crisp, D., Eldering, A., ... Schimel, D. (2017). Influence of El Niño on atmospheric CO2 over the tropical Pacific Ocean: Findings from NASA's OCO-2 mission. *Science*, *358*(6360).

Chung, C.-F. (1996a). Estimating a generalized long memory process. *Journal of econometrics*, *73*(1), 237–259.

Chung, C.-F. (1996b). A generalized fractionally integrated autoregressive moving-average process. *Journal of Time Series Analysis*, *17*(2), 111-140.

Dalla, V., and Hidalgo, J. (2005). A parametric bootstrap test for cycles. *Journal of Econometrics*, *129*(1-2), 219–261.

Davidson, J., and Sibbertsen, P. (2005). Generating schemes for long memory processes: regimes, aggregation and linearity. *Journal of econometrics*, *128*(2), 253–282.

Davidson, J., Stephenson, D., and Turasie, A. (2016). Time series modeling of paleoclimate data. *Environmetrics*, *27*(1), 55–65.

Dettinger, M. D., and Ghil, M. (1998). Seasonal and interannual variations of atmospheric CO2 and climate. *Tellus B*, *50*(1), 1–24.

Dissanayake, G., Peiris, M., Proietti, T., et al. (2018). Fractionally differenced Gegenbauer processes with long memory: a review. *Statistical Science*, *33*(3), 413–426.

Ditlevsen, P., Mitsui, T., and Crucifix, M. (2020). Crossover and peaks in the pleistocene climate spectrum; understanding from simple ice age models. *Climate Dynamics*, *54*(3), 1801–1818.

Doornik, J. A., and Ooms, M. (2003). Computational aspects of maximum likelihood estimation of autoregressive fractionally integrated moving average models. *Computational Statistics & Data Analysis*, *42*(3), 333–348.

Durbin, J. (1960). The fitting of time-series models. *Revue de l'Institut International de Statistique*, 233–244.

Ferrara, L., and Guégan, D. (2001). Forecasting with k-factor Gegenbauer processes: Theory and applications. *Journal of Forecasting*, *20*(8), 581–601.

Forkel, M., Carvalhais, N., Rödenbeck, C., Keeling, R., Heimann, M., Thonicke, K., ... Reichstein, M. (2016). Enhanced seasonal CO2 exchange caused by amplified plant productivity in northern ecosystems. *Science*, *351*(6274), 696–699.

Gil-Alana, L. A. (2017). Alternative modelling approaches for the ENSO time series: persistence and seasonality. *International Journal of Climatology*, *37*(5), 2354–2363.

Giraitis, L., Hidalgo, J., Robinson, P. M., et al. (2001). Gaussian estimation of parametric spectral density with unknown pole. *Annals of Statistics*, *29*(4), 987–1023.

Giraitis, L., and Leipus, R. (1995). A generalized fractionally differencing approach in long-memory modeling. *Lithuanian Mathematical Journal*, *35*(1), 53–65.

Gonçalves, E., and Gourieroux, C. (1988). Agrégation de processus autorégressifs d'ordre 1. *Annales d'Economie et de Statistique*, 127–149.

Granger, C. W. J. (1980). Long memory relationships and the aggregation of dynamic models. *Journal of Econometrics*, *14*(2), 227-238.

Graven, H., Keeling, R., Piper, S., Patra, P., Stephens, B., Wofsy, S., ... others (2013). Enhanced seasonal exchange of CO2 by northern ecosystems since 1960. *Science*, *341*(6150), 1085–1089.

Gray, H. L., Zhang, N.-F., and Woodward, W. A. (1989). On generalized fractional processes. *Journal of time series analysis*, *10*(3), 233–257.

Haldrup, N., and Vera-Valdés, E. (2017). Long memory, fractional integration, and cross sectional aggregation. *Journal of Econometrics*, *199*(1), 1–11.

Hannan, E. J. (1964). The estimation of a changing seasonal pattern. *Journal of the American Statistical Association*, *59*(308), 1063–1077.

Hannan, E. J. (1973). The estimation of frequency. *Journal of Applied probability*, 510–519.

Hassler, U. (1994). (Mis)specification of long memory in seasonal time series. *Journal of Time Series Analysis*, *15*(1), 19–30.

Hays, J. D., Imbrie, J., Shackleton, N. J., et al. (1976). Variations in the earthâFIXME™s orbit: pacemaker of the ice ages. *science*, *194*(4270), 1121–1132.

Hendry, D. F., and Pretis, F. (2013). Anthropogenic influences on atmospheric CO2. In *Handbook on energy and climate change.* Edward Elgar Publishing.

Hosking, J. R. M. (1981, 04). Fractional differencing. *Biometrika*, *68*(1), 165-176.

Hosoya, Y. (1997). A limit theory for long-range dependence and statistical inference on related models. *The Annals of Statistics*, 105–137.

Jouzel, J., Masson-Delmotte, V., Cattani, O., Dreyfus, G., Falourd, S., Hoffmann, G., ... others (2007). Orbital and millennial antarctic climate variability over the past 800,000 years. *science*, *317*(5839), 793–796.

Kaufmann, R. K. (2007). Monthly changes in atmospheric carbon dioxide at Mauna Loa: Possible asymmetric effects of warming. *Earth Interactions*, *11*(10), 1–16.

Kaufmann, R. K., and Juselius, K. (2013). Testing hypotheses about glacial cycles against the observational record. *Paleoceanography*, *28*(1), 175–184.

Kaufmann, R. K., and Juselius, K. (2016). Testing competing forms of the Milankovitch hypothesis: A multivariate approach. *Paleoceanography*, *31*(2), 286–297.

Kaufmann, R. K., and Pretis, F. (2020). Testing hypotheses about glacial dynamics and the stage 11 paradox using a statistical model of paleo-climate. *Climate of the Past Discussions*, 1–28.

Kaufmann, R. K., and Pretis, F. (2021). Understanding glacial cycles: A multivariate disequilibrium approach. *Quaternary Science Reviews*, *251*, 106694.

Keeling, C. D., Bacastow, R. B., Bainbridge, A. E., Ekdahl Jr, C. A., Guenther, P. R., Waterman, L. S., and Chin, J. F. (1976). Atmospheric carbon dioxide variations at Mauna Loa observatory, Hawaii. *Tellus*, *28*(6), 538–551.

Keeling, C. D., Chin, J., and Whorf, T. (1996). Increased activity of northern vegetation inferred from atmospheric CO2 measurements. *Nature*, *382*(6587), 146–149.

Koopman, S. J., Ooms, M., and Carnero, M. A. (2007). Periodic seasonal Reg-ARFIMA–GARCH models for daily electricity spot prices. *Journal of the American Statistical Association*, *102*(477), 16–27.

Lapsa, P. M. (1997). Determination of Gegenbauer-type random process models. *Signal Processing*, *63*(1), 73–90.

Leschinski, C., and Sibbertsen, P. (2019). Model order selection in periodic long memory models. *Econometrics and statistics*, *9*, 78–94.

Levinson, N. (1946). The Wiener (root mean square) error criterion in filter design and prediction. *Journal of Mathematics and Physics*, *25*(1-4), 261–278.

Li, T.-H. (2013). *Time series with mixed spectra*. CRC Press.

Lippi, M., and Zaffaroni, P. (1998). Aggregation of simple linear dynamics: exact asymptotic results. *LSE STICERD Research Paper No. EM350*.

Lisiecki, L. E., and Raymo, M. E. (2005). A pliocene-pleistocene stack of 57 globally distributed benthic δ 18o records. *Paleoceanography*, *20*(1).

Loulergue, L., Schilt, A., Spahni, R., Masson-Delmotte, V., Blunier, T., Lemieux, B., ... Chappellaz, J. (2008). Orbital and millennial-scale features of atmospheric CH 4 over the past 800,000 years. *Nature*, *453*(7193), 383–386.

Lüthi, D., Le Floch, M., Bereiter, B., Blunier, T., Barnola, J.-M., Siegenthaler, U., ... others (2008). High-resolution carbon dioxide concentration record 650,000–800,000 years before present. *Nature*, *453*(7193), 379–382.

Mann, M. E., and Lees, J. M. (1996). Robust estimation of background noise and signal detection in climatic time series. *Climatic change*, *33*(3), 409–445.

McElroy, T. S., and Holan, S. H. (2012). On the computation of autocovariances for generalized Gegenbauer processes. *Statistica Sinica*, 1661–1687.

McElroy, T. S., and Holan, S. H. (2016). Computation of the autocovariances for time series with multiple long-range persistencies. *Computational Statistics & Data Analysis*, *101*, 44–56.

Meyers, S. R., Sageman, B. B., and Pagani, M. (2008). Resolving Milankovitch: Consideration of signal and noise. *American Journal of Science*, *308*(6), 770–786.

Mitchell, J. M. (1976). An overview of climatic variability and its causal mechanisms. *Quaternary Research*, *6*(4), 481–493.

Muller, R. A., and MacDonald, G. J. (1997). Glacial cycles and astronomical forcing. *Science*, *277*(5323), 215–218.

Oppenheim, G., and Viano, M.-C. (2004). Aggregation of random parameters Ornstein-Uhlenbeck or AR processes: some convergence results. *Journal of Time Series Analysis*, *25*(3), 335–350.

Paillard, D. (2001). Glacial cycles: toward a new paradigm. *Reviews of Geophysics*, *39*(3), 325–346.

Palma, W. (2007). *Long-memory time series: theory and methods* (Vol. 662). John Wiley & Sons.

Palma, W., and Chan, N. H. (2005). Efficient estimation of seasonal long-range-dependent processes. *Journal of Time Series Analysis*, *26*(6), 863–892.

Percival, D. B., and Walden, A. T. (2020). *Spectral analysis for univariate time series* (Vol. 51). Cambridge University Press.

Porter-Hudak, S. (1990). An application of the seasonal fractionally differenced model to the monetary aggregates. *Journal of the American Statistical Association*, *85*(410), 338–344.

Pourahmadi, M. (2001). *Foundations of time series analysis and prediction theory* (Vol. 379). John Wiley & Sons.

Proietti, T. (2016). Component-wise representations of long-memory models and volatility prediction. *Journal of Financial Econometrics*, *14*(4), 668–692.

Proietti, T., and Giovannelli, A. (2018). A Durbin–Levinson regularized estimator of high-dimensional autocovariance matrices. *Biometrika*, *105*(4), 783–795.

Quinn, B. G. (2012). The estimation of frequency. In *Handbook of statistics* (Vol. 30, pp. 585–621). Elsevier.

Quinn, B. G., and Hannan, E. J. (2001). *The estimation and tracking of frequency* (No. 9). Cambridge University Press.

Robinson, P. M. (1994). Efficient tests of nonstationary hypotheses. *Journal of the american statistical association*, *89*(428), 1420–1437.

Schennach, S. M. (2018). Long memory via networking. *Econometrica*, *86*(6), 2221–2248.

Smyth, G. K., and Verbyla, A. P. (1996). A conditional likelihood approach to residual maximum likelihood estimation in generalized linear models. *Journal of the Royal Statistical Society: Series B (Methodological)*, *58*(3), 565–572.

Surgailis, D., Koul, H. L., and Giraitis, L. (2012). *Large sample inference for long memory processes*. World Scientific Publishing Company.

Thomson, D. J. (1982). Spectrum estimation and harmonic analysis. *Proceedings of the IEEE*, *70*(9), 1055–1096.

Verbyla, A. P. (1990). A conditional derivation of residual maximum likelihood. *Australian Journal of Statistics*, *32*(2), 227–230.

Wang, K., Wang, Y., Wang, X., He, Y., Li, X., Keeling, R. F., ... others (2020). Causes of slowing-down seasonal CO2 amplitude at Mauna Loa. *Global change biology*, *26*(8), 4462–4477.

Whittle, P. (1953). Estimation and information in stationary time series. *Arkiv för matematik*, *2*(5), 423–434.

Woodward, W. A., Cheng, Q. C., and Gray, H. L. (1998). A k-Factor GARMA long-memory model. *Journal of Time Series Analysis*, *19*(4), 485-504.

Woodward, W. A., Gray, H. L., and Elliott, A. C. (2017). *Applied time series analysis with r*. CRC press.

Wunsch, C. (2003). The spectral description of climate change including the 100 ky energy. *Climate Dynamics*, *20*(4), 353–363.

Zeng, N., Mariotti, A., and Wetzel, P. (2005). Terrestrial mechanisms of interannual CO2 variability. *Global biogeochemical cycles*, *19*(1).

A Mixed spectrum estimation

This appendix deals with maximum likelihood estimation of the parameters of the simplest mixed spectrum process $y_t = \alpha\cos(\lambda t)+\alpha^*\sin(\lambda t)+\epsilon_t$, where $\alpha \sim \mathrm{N}(0,\sigma_\alpha^2)$, $\alpha_t^* \sim \mathrm{N}(0,\sigma_\alpha^2)$, $\mathrm{E}(\alpha\alpha^*) = 0$, $\epsilon_t \sim \mathrm{N}(0,\sigma_\epsilon^2)$. We do not discuss the estimation of λ, for which we refer to Hannan (1973), Quinn (2012), and Percival and Walden (2020, ch. 10), and we assume that λ is a known frequency in the range $(0,\pi)$.

In particular, we are concerned on the MLE of σ_α^2 from a sample realization consisting of n observations $\{y_t, t = 0,1,\ldots,n-1\}$. With obvious notation, $\mathbf{y} \sim \mathrm{N}(\mathbf{0},\boldsymbol{\Gamma}_n)$, $\boldsymbol{\Gamma}_n = \sigma_\epsilon^2\mathbf{I}_n + \sigma_\alpha^2\mathbf{X}\mathbf{X}'$, where we denoted

$$\mathbf{X}' = \begin{pmatrix} 1 & \cos(\lambda) & \ldots & \cos((n-1)\lambda) \\ 0 & \sin(\lambda) & \ldots & \sin((n-1)\lambda) \end{pmatrix}.$$

We will use the approximation $\mathbf{X}'\mathbf{X} = (n/2)\mathbf{I}_2$, which holds exactly if λ coincides with a Fourier frequency, and denote $\varsigma_\alpha = \sigma_\alpha^2/\sigma_\epsilon^2$. Then, we can write

$$|\boldsymbol{\Gamma}_n| = \sigma_\epsilon^{2n}\left(1+\varsigma_\alpha\frac{n}{2}\right)^2, \quad \boldsymbol{\Gamma}_n^{-1} = \frac{1}{\sigma_\epsilon^2}\left(\mathbf{I}_n - \frac{\varsigma_\alpha}{1+\varsigma_\alpha\frac{n}{2}}\mathbf{X}\mathbf{X}'\right).$$

Differentiating the log-likelihood $\ell(\varsigma_\alpha,\sigma_\epsilon^2) = -\frac{n}{2}\log(2\pi) - \frac{1}{2}\log|\boldsymbol{\Gamma}_n| - \frac{1}{2}\mathbf{y}'\boldsymbol{\Gamma}_n^{-1}\mathbf{y}$ with respect to the parameters and equating to zero yields

$$\tilde{\varsigma}_\alpha = \frac{\mathrm{ESS}}{n\tilde{\sigma}_\epsilon^2} - \frac{2}{n}, \quad \tilde{\sigma}_\epsilon^2 = \frac{\mathrm{RSS}}{n} - \frac{1}{1+\tilde{\varsigma}_\alpha\frac{n}{2}}\frac{\mathrm{ESS}}{n},$$

where $\mathrm{ESS} = \mathbf{y}'\mathbf{X}(\mathbf{X}'\mathbf{X})^{-1}\mathbf{X}'\mathbf{y}$ is the explained sum of squares of the regression of y_t on $\mathbf{x}_t = (\cos(\lambda t),\sin(\lambda t))'$ and $\mathrm{RSS} = \mathbf{y}'\mathbf{y} - \mathbf{y}'\mathbf{X}(\mathbf{X}'\mathbf{X})^{-1}\mathbf{X}'\mathbf{y}$ is the corresponding residual sum of squares. Hence, for n large, σ_α^2 is estimated as ESS/n.

The Hessian matrix has elements

$$\frac{\partial^2\ell}{\partial(\sigma_\epsilon^2)^2} = O(n), \frac{\partial^2\ell}{\partial\sigma_\epsilon^2\partial\varsigma_\alpha} = O(1), \frac{\partial^2\ell}{\partial\varsigma_\alpha^2} = O(1),$$

and in particular $\frac{\partial^2\ell}{\partial\varsigma_\alpha^2}|_{\varsigma_\alpha=\tilde{\varsigma}_\alpha} = \frac{2}{\left(\frac{2}{n}+\tilde{\varsigma}_\alpha\right)^2}$, so that the sample information on ς_α does not increase with n.

B Parametric bootstrap and simulation

The Durbin-Levinson algorithm of section 5 provides the factorization of the precision matrix $\boldsymbol{\Gamma}_n^{-1} = \boldsymbol{\Phi}_n'\mathbf{D}_n\boldsymbol{\Phi}_n$. Denoting $\tilde{\mathbf{u}} = \mathbf{y} - \mathbf{X}\tilde{\boldsymbol{\beta}}$, a bootstrap sample $\mathbf{y}^*$ is drawn as follows.

1. Compute the scaled residuals $\mathbf{e} = \mathbf{D}_n^{1/2}\boldsymbol{\Phi}_n\tilde{\mathbf{u}}$. The vector $\mathbf{e}$ has elements

$$e_t = \left(\tilde{u}_t - \sum_{j=1}^{t-1}\tilde{\phi}_{t-1,j}\tilde{u}_{t-j}\right)/\sqrt{\tilde{v}_{t-1}}, t = 2,\ldots,n, \;\; e_1 = \tilde{u}_1/\sqrt{\tilde{v}_0}.$$

2. Sample $\mathbf{e}$ with replacement; let $\mathbf{e}^*$ denote the bootstrap sample.

3. Compute the bootstrap sample $\mathbf{y}^* = \mathbf{X}\tilde{\boldsymbol{\beta}} + \mathbf{u}^*$ where, using $\boldsymbol{\Phi}_n \mathbf{u}^* = \mathbf{D}_n^{-1/2}\mathbf{e}^*$, the elements of $\mathbf{u}^*$ are obtained recursively as follows:

$$\begin{aligned}
u_1^* &= \sqrt{v_0}e_1^* \\
u_2^* &= \phi_{1,1}u_1^* + \sqrt{v_1}e_2^* \\
u_3^* &= \phi_{2,1}u_2^* + \phi_{2,2}u_1^* + \sqrt{v_2}e_3^* \\
&\vdots \\
u_t^* &= \phi_{t-1,1}u_{t-1}^* + \cdots + \phi_{t-1,t-1}u_1^* + \sqrt{v_{t-1}}e_t^* \\
&\vdots \\
u_n^* &= \phi_{n-1,1}u_{n-1}^* + \cdots + \phi_{n-1,n-1}u_1^* + \sqrt{v_{n-1}}e_n^*
\end{aligned}$$

Simularly, to simulate from the Gaussian process $\mathbf{y}|\mathbf{X} \sim \mathrm{N}(\mathbf{X}\boldsymbol{\beta}, \boldsymbol{\Gamma}_n)$, we skip step 1 of the above sampling scheme and replace step 2 by drawing $\mathbf{e}^* \sim \mathrm{N}(\mathbf{0}, \mathbf{I}_n)$, and replace $\tilde{\boldsymbol{\beta}}$ with the true $\boldsymbol{\beta}$.

C Simulation study

This appendix reports the result of a Monte Carlo experiment for assessing the finite sample properties of the maximum likelihood estimators of the parameters d, λ and σ_η^2 of the basic fSW model (1). The objective is also to compare the exact MLE with the approximate MLE based on the Whittle approximation to the log-likelihood funciton. In both cases, the MLE is computed by maximising the log-likelihood numerically using a Quasi-Newton algorithm of transformed parameters $\vartheta_1 = \log((0.5+d)/(0.5-d))$, $\vartheta_2 = \log(2\pi/\lambda - 2)$ and $\vartheta_3 = 0.5\log(\sigma_\eta^2)$.

The design of the experiment considers four sample sizes, $n = \{100, 250, 500, 1000\}$, six values of the memory parameter, $d = \{0.10, 0.20,\ 0.30, 0.40, 0.45, 0.49\}$, six frequencies $\lambda = \{\pi/50, \pi/25, \pi/15, \pi/3,\ \pi/2, \pi\}$, and we set $\sigma_\eta^2 = 1$ throughout. The Monte Carlo results reported below are computed across 1,000 replications of the experiment. Note that in the case $\lambda = \pi$ the model is $y_t = \alpha_t^* \cos(\pi t)$, i.e., the sine term vanishes.

Gray et al. (1989), Chung (1996a) and Giraitis et al. (2001) estimate λ by a grid search. In particular, Chung (1996a) discusses the problems in the convergence of gradient based algorithms, ascribing them to the different convergence rates of the MLEs of d and λ. We found that these problems are remedied by choosing suitable initial values. For the frequency parameter we consider the $\hat{\lambda} = \mathrm{argmax}_\omega I(\omega)$, i.e. the frequency corresponding to the largest periodogram value, see Quinn (2012); for the memory parameter d we consider the Arteche and Robinson (2000) semi-parametric estimator

$$\hat{d} = -\frac{1}{2}\frac{\sum_{j=\pm 1}^{\pm\lfloor n^{0.75}\rfloor} \nu_j \log I(\hat{\lambda}+\omega_j)}{\sum_{j=\pm 1}^{\pm\lfloor n^{0.75}\rfloor} \nu_j^2},$$

where $\nu_j = \log|j| + \frac{1}{n^{0.75}}\sum_{h=1}^{\lfloor n^{0.75}\rfloor}\log h$; for σ_η^2 we consider the sample variance s^2 scaled by $\Gamma^2(1-\hat{d})/\Gamma(1-2\hat{d})$. The optimization is performed in MATLAB-R 2019a using the function `fminunc`.

Tables 4–6 report the Monte Carlo estimates of the bias and the root mean square error of the exact and Whittle MLEs of d, λ and σ_η^2. Table 7 reports the average integrated square distance between the theoretical log-spectrum and the estimated one, defined as

$$\mathcal{D}_n = \int_{-\pi}^{\pi}\left(\log f(\omega;\theta) - \log f(\omega;\tilde{\theta})\right)^2 d\omega,$$

where $\theta = [d, \lambda, \sigma_\eta^2]'$ and $\mathcal{D}_n$ is approximated via numerical integration.

The synthetic evidence is that the exact MLE is more accurate for the estimation of the parameters and the spectral density, except for the case when $n = 100$ and the memory is low. Finally, we considered the likelihood approximation obtained by the regularized Durbin-Levinson proposed in Proietti and Giovannelli (2018). This approach led to result, not reported for brevity, very close to exact MLE; they seem to suggest that for large n the approximation can be suitable and very effective in enhancing computational speed.

Table 4: Bias and RMSE of the exact and Whittle maximum likelihood estimators of the memory parameter d of an fSW process.

Bias

		Exact likelihood						Whittle likelihood					
		$\lambda=\pi/50$	$\lambda=\pi/25$	$\lambda=\pi/15$	$\lambda=\pi/3$	$\lambda=\pi/2$	$\lambda=\pi$	$\lambda=\pi/50$	$\lambda=\pi/25$	$\lambda=\pi/15$	$\lambda=\pi/3$	$\lambda=\pi/2$	$\lambda=\pi$
n=100	$d=0.10$	-0.0837	-0.0593	-0.0427	0.0034	0.0094	0.0129	-0.0079	-0.0328	-0.0384	-0.0482	-0.0398	-0.0500
	$d=0.20$	-0.1951	-0.1469	-0.0723	-0.0243	-0.0275	-0.0105	-0.0297	-0.0572	-0.0747	-0.0797	-0.0779	-0.0620
	$d=0.30$	-0.2206	-0.1237	-0.0610	-0.0270	-0.0265	-0.0179	-0.0272	-0.0440	-0.0971	-0.0586	-0.0421	-0.0471
	$d=0.40$	-0.1156	-0.0508	-0.0312	-0.0255	-0.0210	-0.0294	-0.0102	-0.0830	-0.1448	-0.0093	0.0007	-0.0350
	$d=0.45$	-0.0646	-0.0308	-0.0244	-0.0220	-0.0244	-0.0326	-0.0191	-0.1477	-0.1814	0.0124	-0.0027	-0.0384
	$d=0.49$	-0.0251	-0.0165	-0.0137	-0.0147	-0.0136	-0.0266	-0.1113	-0.2342	-0.0879	0.0017	-0.0192	-0.0395
n=250	$d=0.10$	-0.0066	-0.0089	-0.0130	-0.0049	-0.0053	-0.0086	-0.0520	-0.0580	-0.0642	-0.0522	-0.0583	-0.0514
	$d=0.20$	-0.0177	-0.0158	-0.0138	-0.0238	-0.0217	-0.0166	-0.0727	-0.0883	-0.1038	-0.0655	-0.0713	-0.0482
	$d=0.30$	-0.0083	-0.0116	-0.0106	-0.0200	-0.0149	-0.0194	-0.1109	-0.1210	-0.1008	-0.0306	-0.0249	-0.0319
	$d=0.40$	-0.0112	-0.0113	-0.0102	-0.0142	-0.0130	-0.0193	-0.0893	-0.0937	-0.0330	0.0123	0.0236	-0.0169
	$d=0.45$	-0.0134	-0.0131	-0.0118	-0.0143	-0.0133}	-0.0194	-0.0321	-0.0810	0.0031	0.0230	0.0294	-0.0117
	$d=0.49$	-0.0100	-0.0093	-0.0095	-0.0110	-0.0101	-0.0171	-0.0008	-0.0987	0.0033	0.0065	0.0086	-0.0163
n=500	$d=0.10$	-0.0222	-0.0245	-0.0238	-0.0228	-0.0193	-0.0188	-0.0576	-0.0632	-0.0656	-0.0597	-0.0691	-0.0495
	$d=0.20$	-0.0114	-0.0094	-0.0105	-0.0198	-0.0167	-0.0113	-0.0922	-0.0885	-0.0926	-0.0520	-0.0735	-0.0345
	$d=0.30$	-0.0052	-0.0063	-0.0051	-0.0090	-0.0103	-0.0075	-0.0708	-0.0571	-0.0463	-0.0128	-0.0287	-0.0124
	$d=0.40$	-0.0066	-0.0074	-0.0057	-0.0063	-0.0075	-0.0102	-0.0160	-0.0151	0.0076	0.0143	-0.0138	-0.0068
	$d=0.45$	-0.0099	-0.0070	-0.0093	-0.0082	-0.0094	-0.0128	-0.0139	-0.0109	0.0200	0.0243	-0.0102	-0.0052
	$d=0.49$	-0.0096	-0.0078	-0.0081	-0.0079	-0.0087	-0.0125	-0.0217	-0.0320	0.0079	0.0070	-0.0411	-0.0088
n=1000	$d=0.10$	-0.0236	-0.0243	-0.0317	-0.0349	-0.0300	-0.0204	-0.0597	-0.0631	-0.0681	-0.0659	-0.0715	-0.0447
	$d=0.20$	-0.0036	-0.0054	-0.0053	-0.0102	-0.0106	-0.0038	-0.0621	-0.0607	-0.0760	-0.0394	-0.0593	-0.0165
	$d=0.30$	-0.0039	-0.0045	-0.0021	-0.0054	-0.0040	-0.0057	-0.0135	-0.0160	-0.0208	-0.0065	-0.0172	-0.0075
	$d=0.40$	-0.0046	-0.0035	-0.0036	-0.0035	-0.0051	-0.0071	-0.0012	-0.0013	0.0067	0.0113	-0.0060	-0.0049
	$d=0.45$	-0.0051	-0.0043	-0.0050	-0.0045	-0.0050	-0.0072	0.0028	0.0012	0.0208	0.0215	-0.0092	-0.0019
	$d=0.49$	-0.0065	-0.0061	-0.0063	-0.0059	-0.0066	-0.0084	-0.0067	-0.0173	0.0081	0.0075	-0.0343	-0.0046

Root mean square error

		Exact likelihood						Whittle likelihood					
		$\lambda=\pi/50$	$\lambda=\pi/25$	$\lambda=\pi/15$	$\lambda=\pi/3$	$\lambda=\pi/2$	$\lambda=\pi$	$\lambda=\pi/50$	$\lambda=\pi/25$	$\lambda=\pi/15$	$\lambda=\pi/3$	$\lambda=\pi/2$	$\lambda=\pi$
n=100	$d=0.10$	0.8374	0.8235	0.8149	0.7862	0.7785	0.7696	0.8078	0.7972	0.7916	0.7772	0.7714	0.7642
	$d=0.20$	0.8778	0.8621	0.8257	0.7797	0.7723	0.7555	0.8191	0.8199	0.8074	0.7922	0.7993	0.7691
	$d=0.30$	0.8947	0.8607	0.8194	0.7502	0.7430	0.7269	0.8071	0.8172	0.8230	0.7861	0.7880	0.7667
	$d=0.40$	0.8605	0.8078	0.7736	0.7136	0.7062	0.7178	0.7874	0.8300	0.8427	0.7625	0.7609	0.7532
	$d=0.45$	0.8257	0.7566	0.7245	0.7129	0.6973	0.7127	0.7843	0.8459	0.8518	0.7247	0.7368	0.7465
	$d=0.49$	0.7610	0.7152	0.6426	0.6551	0.6474	0.6912	0.8285	0.8634	0.8127	0.6639	0.7085	0.7305
n=250	$d=0.10$	0.5593	0.5604	0.5528	0.5365	0.5327	0.5552	0.5495	0.5497	0.5566	0.5444	0.5515	0.5424
	$d=0.20$	0.5575	0.5499	0.5361	0.5535	0.5292	0.5483	0.5985	0.6037	0.6159	0.5832	0.5867	0.5575
	$d=0.30$	0.4577	0.4705	0.4723	0.5075	0.4926	0.5293	0.6479	0.6489	0.6365	0.5539	0.5512	0.5375
	$d=0.40$	0.4451	0.4451	0.4416	0.4580	0.4568	0.4735	0.6662	0.6517	0.6052	0.5126	0.5246	0.4995
	$d=0.45$	0.4352	0.4303	0.4275	0.4392	0.4326	0.4597	0.6256	0.6376	0.5555	0.4723	0.4745	0.4771
	$d=0.49$	0.3808	0.3755	0.3782	0.3922	0.3811	0.4259	0.4937	0.6357	0.4508	0.3625	0.3413	0.4473
n=500	$d=0.10$	0.3267	0.3131	0.3269	0.2741	0.2588	0.3092	0.2916	0.2925	0.2950	0.2935	0.2971	0.2769
	$d=0.20$	0.2752	0.2408	0.2843	0.2693	0.2442	0.2590	0.3495	0.3454	0.3507	0.3038	0.3263	0.2704
	$d=0.30$	0.1798	0.1754	0.1982	0.1893	0.2051	0.2078	0.3593	0.3360	0.3230	0.2301	0.2755	0.2293
	$d=0.40$	0.1700	0.1689	0.1674	0.1711	0.1754	0.1854	0.2785	0.2621	0.2432	0.2104	0.2409	0.1986
	$d=0.45$	0.1697	0.1577	0.1627	0.1599	0.1633	0.1836	0.2684	0.2532	0.2161	0.1996	0.2300	0.1951
	$d=0.49$	0.1389	0.1296	0.1282	0.1328	0.1340	0.1548	0.2487	0.2715	0.1223	0.1106	0.2644	0.1630
n=1000	$d=0.10$	0.0876	0.0934	0.1011	0.0749	0.0634	0.0900	0.0758	0.0801	0.0826	0.0826	0.0837	0.0668
	$d=0.20$	0.0335	0.0471	0.0414	0.0470	0.0453	0.0244	0.0940	0.0926	0.1018	0.0722	0.0878	0.0439
	$d=0.30$	0.0241	0.0221	0.0217	0.0242	0.0256	0.0258	0.0529	0.0538	0.0672	0.0358	0.0523	0.0298
	$d=0.40$	0.0221	0.0204	0.0204	0.0223	0.0231	0.0265	0.0295	0.0325	0.0411	0.0309	0.0359	0.0270
	$d=0.45$	0.0197	0.0199	0.0186	0.0197	0.0198	0.0251	0.0265	0.0308	0.0355	0.0343	0.0412	0.0275
	$d=0.49$	0.0139	0.0135	0.0135	0.0133	0.0137	0.0181	0.0308	0.0477	0.0118	0.0106	0.0565	0.0193

Table 5: Bias and RMSE of the exact and Whittle maximum likelihood estimators of the frequency parameter λ of an fSW process.

Bias

		Exact likelihood						Whittle likelihood					
		$\lambda=\pi/50$	$\lambda=\pi/25$	$\lambda=\pi/15$	$\lambda=\pi/3$	$\lambda=\pi/2$	$\lambda=\pi$	$\lambda=\pi/50$	$\lambda=\pi/25$	$\lambda=\pi/15$	$\lambda=\pi/3$	$\lambda=\pi/2$	$\lambda=\pi$
n=100	$d=0.10$	1.4131	1.3057	1.1431	0.4824	0.2036	-0.8321	0.9876	0.9583	0.8388	0.3334	0.0435	-0.9597
	$d=0.20$	1.1047	0.9300	0.5912	0.1695	0.0901	-0.3350	0.4650	0.4615	0.3371	0.0707	0.0040	-0.4031
	$d=0.30$	0.8048	0.4771	0.2457	0.0324	0.0173	-0.1197	0.1385	0.0932	0.0560	0.0034	-0.0128	-0.1551
	$d=0.40$	0.3481	0.1204	0.0516	0.0027	0.0055	-0.0446	0.0079	-0.0193	-0.0373	-0.0056	-0.0068	-0.0646
	$d=0.45$	0.1502	0.0374	0.0136	0.0044	0.0018	-0.0244	-0.0335	-0.0393	-0.0363	-0.0019	-0.0087	-0.0400
	$d=0.49$	0.0379	0.0118	0.0002	-0.0015	-0.0002	-0.0110	-0.0381	-0.0369	-0.0267	-0.0014	-0.0024	-0.0182
n=250	$d=0.10$	0.7627	0.7682	0.7606	0.2643	0.0713	-0.7137	0.7188	0.7336	0.7100	0.2142	0.0131	-0.7941
	$d=0.20$	0.1970	0.1842	0.1326	0.0627	0.0174	-0.2108	0.1731	0.1550	0.1138	0.0472	0.0071	-0.2246
	$d=0.30$	0.0234	0.0141	0.0032	0.0005	-0.0009	-0.0613	0.0084	0.0035	-0.0079	-0.0051	-0.0099	-0.0691
	$d=0.40$	0.0046	0.0008	-0.0024	-0.0005	0.0014	-0.0204	0.0009	-0.0029	-0.0086	-0.0052	-0.0114	-0.0274
	$d=0.45$	0.0013	0.0002	-0.0001	-0.0008	-0.0004	-0.0106	-0.0027	-0.0014	-0.0068	-0.0075	-0.0156	-0.0180
	$d=0.49$	0.0005	-0.0004	-0.0002	0.0000	0.0002	-0.0038	-0.0027	-0.0007	-0.0086	0.0000	-0.0113	-0.0070
n=500	$d=0.10$	0.6292	0.6301	0.5510	0.2131	0.0179	-0.5794	0.5940	0.5986	0.5169	0.1844	-0.0279	-0.6350
	$d=0.20$	0.1033	0.0579	0.0610	0.0221	0.0014	-0.1044	0.0938	0.0529	0.0575	0.0169	-0.0106	-0.1212
	$d=0.30$	0.0080	0.0029	-0.0015	0.0015	0.0014	-0.0227	0.0062	0.0014	-0.0022	-0.0015	-0.0029	-0.0254
	$d=0.40$	0.0013	0.0001	-0.0017	-0.0001	-0.0007	-0.0102	-0.0009	-0.0016	-0.0019	-0.0037	-0.0018	-0.0151
	$d=0.45$	-0.0002	0.0001	-0.0001	0.0002	0.0001	-0.0064	-0.0012	-0.0008	0.0007	-0.0067	-0.0008	-0.0116
	$d=0.49$	0.0000	0.0000	0.0000	0.0000	0.0000	-0.0017	-0.0003	-0.0001	0.0023	-0.0064	-0.0008	-0.0045
n=1000	$d=0.10$	0.4933	0.4299	0.4702	0.1735	-0.0061	-0.4386	0.4681	0.4128	0.4438	0.1597	-0.0250	-0.4737
	$d=0.20$	0.0354	0.0272	0.0159	-0.0069	-0.0031	-0.0366	0.0350	0.0255	0.0185	-0.0067	-0.0034	-0.0382
	$d=0.30$	0.0020	-0.0017	-0.0017	-0.0001	-0.0001	-0.0119	0.0009	-0.0033	-0.0035	-0.0012	0.0002	-0.0137
	$d=0.40$	0.0001	0.0000	-0.0001	0.0000	-0.0002	-0.0044	-0.0008	-0.0008	-0.0024	-0.0002	-0.0006	-0.0064
	$d=0.45$	-0.0002	0.0000	0.0000	0.0001	0.0000	-0.0022	-0.0010	-0.0004	-0.0018	-0.0002	-0.0003	-0.0055
	$d=0.49$	0.0000	0.0000	-0.0001	0.0000	0.0000	-0.0009	-0.0003	-0.0002	-0.0020	0.0003	-0.0003	-0.0031

Root mean square error

		Exact likelihood						Whittle likelihood					
		$\lambda=\pi/50$	$\lambda=\pi/25$	$\lambda=\pi/15$	$\lambda=\pi/3$	$\lambda=\pi/2$	$\lambda=\pi$	$\lambda=\pi/50$	$\lambda=\pi/25$	$\lambda=\pi/15$	$\lambda=\pi/3$	$\lambda=\pi/2$	$\lambda=\pi$
n=100	$d=0.10$	1.0458	1.0355	1.0186	0.9179	0.8384	0.9786	1.0005	0.9964	0.9802	0.8788	0.7723	0.9956
	$d=0.20$	1.0168	0.9959	0.9430	0.8258	0.7908	0.8774	0.9185	0.9173	0.8846	0.7894	0.7871	0.8963
	$d=0.30$	0.9836	0.9281	0.8649	0.7516	0.7407	0.7833	0.8301	0.8253	0.8152	0.7776	0.7843	0.8125
	$d=0.40$	0.9038	0.8236	0.7784	0.7067	0.7012	0.7270	0.7874	0.8229	0.8239	0.7623	0.7610	0.7647
	$d=0.45$	0.8430	0.7584	0.7211	0.7080	0.6882	0.7078	0.7861	0.8276	0.8241	0.7235	0.7373	0.7471
	$d=0.49$	0.7640	0.7140	0.6327	0.6468	0.6388	0.6808	0.8156	0.8202	0.8019	0.6639	0.7044	0.7211
n=250	$d=0.10$	0.9364	0.9381	0.9356	0.7254	0.5726	0.9212	0.9220	0.9266	0.9191	0.6891	0.5198	0.9449
	$d=0.20$	0.6839	0.6729	0.6280	0.5763	0.5274	0.6916	0.6711	0.6550	0.6237	0.5712	0.5550	0.6997
	$d=0.30$	0.4706	0.4720	0.4698	0.5015	0.4886	0.5590	0.6086	0.6001	0.6002	0.5464	0.5469	0.5673
	$d=0.40$	0.4413	0.4403	0.4377	0.4518	0.4516	0.4745	0.6473	0.6266	0.6008	0.5109	0.5195	0.5066
	$d=0.45$	0.4273	0.4220	0.4204	0.4305	0.4243	0.4516	0.6221	0.6160	0.5557	0.4599	0.4583	0.4812
	$d=0.49$	0.3687	0.3641	0.3670	0.3804	0.3689	0.4104	0.4939	0.6006	0.4528	0.3557	0.3524	0.4392
n=500	$d=0.10$	0.7986	0.7982	0.7488	0.4741	0.2580	0.7661	0.7728	0.7755	0.7212	0.4411	0.2483	0.7985
	$d=0.20$	0.3572	0.2853	0.3173	0.2705	0.2393	0.3515	0.3512	0.3097	0.3151	0.2794	0.2787	0.3706
	$d=0.30$	0.1813	0.1739	0.1974	0.1863	0.2021	0.2195	0.3289	0.3121	0.3058	0.2268	0.2652	0.2389
	$d=0.40$	0.1678	0.1660	0.1658	0.1691	0.1727	0.1854	0.2755	0.2589	0.2423	0.2050	0.2375	0.2042
	$d=0.45$	0.1645	0.1545	0.1575	0.1557	0.1580	0.1784	0.2659	0.2514	0.2054	0.1796	0.2279	0.1987
	$d=0.49$	0.1295	0.1219	0.1195	0.1257	0.1254	0.1433	0.2407	0.2576	0.1136	0.1091	0.2378	0.1596
n=1000	$d=0.10$	0.5004	0.4392	0.4799	0.1857	0.0561	0.4473	0.4704	0.4157	0.4462	0.1672	0.0502	0.4762
	$d=0.20$	0.0486	0.0541	0.0440	0.0464	0.0441	0.0438	0.0787	0.0744	0.0702	0.0608	0.0648	0.0558
	$d=0.30$	0.0239	0.0217	0.0217	0.0236	0.0252	0.0279	0.0512	0.0514	0.0640	0.0352	0.0494	0.0319
	$d=0.40$	0.0216	0.0201	0.0200	0.0221	0.0225	0.0259	0.0294	0.0324	0.0406	0.0288	0.0354	0.0273
	$d=0.45$	0.0191	0.0194	0.0179	0.0192	0.0192	0.0242	0.0264	0.0308	0.0289	0.0267	0.0402	0.0280
	$d=0.49$	0.0123	0.0120	0.0120	0.0119	0.0120	0.0160	0.0300	0.0444	0.0088	0.0075	0.0448	0.0190

Table 6: Bias and RMSE of the exact and Whittle maximum likelihood estimators of the disturbance variance parameter σ_η^2 of an fSW process.

Bias

		Exact likelihood						Whittle likelihood					
		$\lambda=\pi/50$	$\lambda=\pi/25$	$\lambda=\pi/15$	$\lambda=\pi/3$	$\lambda=\pi/2$	$\lambda=\pi$	$\lambda=\pi/50$	$\lambda=\pi/25$	$\lambda=\pi/15$	$\lambda=\pi/3$	$\lambda=\pi/2$	$\lambda=\pi$
n=100	$d=0.10$	-0.0515	-0.0465	-0.0402	-0.0489	-0.0451	-0.0293	0.0224	-0.0062	0.0118	-0.0386	-0.0440	-0.0209
	$d=0.20$	-0.0444	-0.0390	-0.0308	-0.0281	-0.0189	-0.0351	0.0720	0.0858	0.1146	0.0081	-0.0068	-0.0409
	$d=0.30$	-0.0249	-0.0250	-0.0239	-0.0146	-0.0120	-0.0223	0.1126	0.2510	0.3953	0.0534	0.0085	-0.0230
	$d=0.40$	0.0124	-0.0040	-0.0205	-0.0010	-0.0071	-0.0249	0.1915	0.8748	0.9223	0.1269	0.0287	-0.0226
	$d=0.45$	0.0155	-0.0097	-0.0140	-0.0018	-0.0010	-0.0242	0.5944	1.9510	1.5733	0.3184	0.0674	-0.0107
	$d=0.49$	0.0258	0.0079	-0.0054	-0.0054	0.0071	-0.0140	7.1101	11.2829	3.1664	5.2504	0.4821	0.0229
n=250	$d=0.10$	-0.0134	-0.0172	-0.0091	-0.0118	-0.0135	-0.0190	0.0298	0.0231	0.0350	-0.0002	-0.0021	-0.0109
	$d=0.20$	-0.0130	-0.0086	-0.0115	-0.0036	-0.0021	-0.0173	0.0731	0.0927	0.0933	0.0220	0.0285	-0.0159
	$d=0.30$	-0.0108	-0.0062	-0.0084	-0.0058	-0.0017	-0.0177	0.1802	0.1789	0.1388	0.0216	0.0337	-0.0239
	$d=0.40$	-0.0089	-0.0119	-0.0081	0.0033	-0.0019	-0.0160	0.3343	0.3564	0.1988	0.0552	0.0515	-0.0163
	$d=0.45$	-0.0015	-0.0058	-0.0084	0.0049	0.0076	-0.0080	0.3843	0.7148	0.2366	0.1529	0.2142	0.0072
	$d=0.49$	-0.0046	-0.0026	-0.0075	0.0033	0.0000	-0.0065	1.1964	4.2428	0.8761	0.8694	1.8403	0.0176
n=500	$d=0.10$	-0.0088	-0.0043	-0.0104	-0.0016	-0.0024	-0.0109	0.0233	0.0266	0.0201	0.0135	0.0152	-0.0016
	$d=0.20$	-0.0058	-0.0086	-0.0075	-0.0016	0.0026	-0.0121	0.0552	0.0455	0.0543	0.0207	0.0453	-0.0113
	$d=0.30$	-0.0021	-0.0035	0.0000	0.0001	-0.0007	-0.0090	0.0935	0.0714	0.0757	0.0207	0.0413	-0.0136
	$d=0.40$	-0.0040	-0.0018	-0.0039	0.0006	-0.0005	-0.0029	0.0746	0.0709	0.0540	0.0218	0.0635	0.0039
	$d=0.45$	-0.0055	-0.0044	-0.0028	0.0009	0.0028	-0.0051	0.1272	0.1356	0.0816	0.0694	0.0952	0.0047
	$d=0.49$	-0.0009	-0.0008	-0.0041	0.0024	0.0043	0.0021	0.3655	1.0703	0.4252	0.4793	0.8353	0.0232
n=1000	$d=0.10$	-0.0013	-0.0044	-0.0048	0.0003	0.0004	-0.0076	0.0201	0.0142	0.0174	0.0147	0.0146	0.0029
	$d=0.20$	-0.0010	0.0002	-0.0030	0.0023	0.0020	-0.0031	0.0350	0.0383	0.0479	0.0267	0.0403	-0.0026
	$d=0.30$	-0.0037	-0.0018	-0.0019	0.0017	-0.0021	-0.0015	0.0117	0.0223	0.0413	0.0167	0.0327	-0.0009
	$d=0.40$	-0.0011	-0.0046	-0.0015	0.0029	0.0024	-0.0006	0.0115	0.0125	0.0312	0.0104	0.0257	0.0043
	$d=0.45$	-0.0013	-0.0021	-0.0008	0.0010	0.0008	-0.0028	0.0098	0.0176	0.0447	0.0218	0.0500	0.0042
	$d=0.49$	0.0005	-0.0028	-0.0006	0.0024	0.0049	-0.0018	0.0392	0.4761	0.2449	0.2657	0.7143	0.0098

Root mean square error

		Exact likelihood						Whittle likelihood					
		$\lambda=\pi/50$	$\lambda=\pi/25$	$\lambda=\pi/15$	$\lambda=\pi/3$	$\lambda=\pi/2$	$\lambda=\pi$	$\lambda=\pi/50$	$\lambda=\pi/25$	$\lambda=\pi/15$	$\lambda=\pi/3$	$\lambda=\pi/2$	$\lambda=\pi$
n=100	$d=0.10$	0.9839	0.9838	0.9842	0.9818	0.9821	0.9840	0.9923	0.9880	0.9902	0.9828	0.9819	0.9849
	$d=0.20$	0.9741	0.9735	0.9718	0.9700	0.9711	0.9682	0.9862	0.9879	0.9909	0.9754	0.9735	0.9673
	$d=0.30$	0.9661	0.9612	0.9570	0.9551	0.9553	0.9533	0.9773	0.9963	1.0133	0.9671	0.9602	0.9539
	$d=0.40$	0.9516	0.9422	0.9367	0.9386	0.9373	0.9339	0.9733	1.0511	1.0552	0.9624	0.9455	0.9353
	$d=0.45$	0.9385	0.9280	0.9260	0.9284	0.9283	0.9235	1.0180	1.1219	1.0994	0.9830	0.9427	0.9273
	$d=0.49$	0.9273	0.9220	0.9182	0.9176	0.9210	0.9166	1.2890	1.3613	1.1769	1.2447	0.9992	0.9254
n=250	$d=0.10$	0.9718	0.9708	0.9728	0.9718	0.9713	0.9702	0.9828	0.9809	0.9840	0.9747	0.9742	0.9718
	$d=0.20$	0.9436	0.9447	0.9436	0.9462	0.9462	0.9421	0.9684	0.9735	0.9737	0.9538	0.9556	0.9423
	$d=0.30$	0.9116	0.9132	0.9125	0.9137	0.9149	0.9102	0.9715	0.9709	0.9598	0.9234	0.9272	0.9083
	$d=0.40$	0.8773	0.8762	0.8775	0.8818	0.8799	0.8749	0.9874	0.9921	0.9485	0.9009	0.8998	0.8752
	$d=0.45$	0.8610	0.8593	0.8582	0.8635	0.8645	0.8586	0.9863	1.0622	0.9435	0.9161	0.9353	0.8649
	$d=0.49$	0.8433	0.8441	0.8421	0.8466	0.8452	0.8427	1.1431	1.4767	1.0852	1.0837	1.2382	0.8528
n=500	$d=0.10$	0.9472	0.9490	0.9464	0.9493	0.9486	0.9455	0.9620	0.9635	0.9601	0.9569	0.9575	0.9489
	$d=0.20$	0.8932	0.8908	0.8925	0.8952	0.8970	0.8892	0.9268	0.9216	0.9264	0.9079	0.9213	0.8896
	$d=0.30$	0.8359	0.8349	0.8373	0.8372	0.8370	0.8321	0.8949	0.8818	0.8839	0.8500	0.8629	0.8296
	$d=0.40$	0.7725	0.7739	0.7725	0.7754	0.7748	0.7733	0.8239	0.8211	0.8103	0.7894	0.8160	0.7779
	$d=0.45$	0.7383	0.7390	0.7401	0.7426	0.7439	0.7388	0.8251	0.8297	0.7956	0.7876	0.8045	0.7457
	$d=0.49$	0.7137	0.7138	0.7114	0.7160	0.7173	0.7159	0.9367	1.2577	0.9671	0.9946	1.1604	0.7306
n=1000	$d=0.10$	0.9027	0.9001	0.9004	0.9027	0.9021	0.8967	0.9212	0.9155	0.9186	0.9161	0.9157	0.9042
	$d=0.20$	0.7997	0.8016	0.7980	0.8036	0.8033	0.7973	0.8380	0.8412	0.8506	0.8289	0.8428	0.7985
	$d=0.30$	0.6967	0.6986	0.6985	0.7021	0.6984	0.6990	0.7136	0.7241	0.7441	0.7175	0.7344	0.6997
	$d=0.40$	0.5993	0.5957	0.5988	0.6033	0.6028	0.6000	0.6122	0.6134	0.6325	0.6111	0.6267	0.6049
	$d=0.45$	0.5491	0.5483	0.5495	0.5513	0.5512	0.5477	0.5605	0.5685	0.5954	0.5725	0.6013	0.5548
	$d=0.49$	0.5106	0.5074	0.5095	0.5126	0.5150	0.5085	0.5500	0.9871	0.7550	0.7757	1.2251	0.5201

Table 7: Average integrated square distance between the true log-spectral density and the that estimated by exact and Whittle likelihood methods.

		Exact likelihood						Whittle likelihood					
		$\lambda = \pi/50$	$\lambda = \pi/25$	$\lambda = \pi/15$	$\lambda = \pi/3$	$\lambda = \pi/2$	$\lambda = \pi$	$\lambda = \pi/50$	$\lambda = \pi/25$	$\lambda = \pi/15$	$\lambda = \pi/3$	$\lambda = \pi/2$	$\lambda = \pi$
n=100	$d = 0.10$	0.2274	0.2306	0.2223	0.1644	0.0909	0.2081	0.2261	0.1937	0.1739	0.0930	0.0429	0.1845
	$d = 0.20$	0.8503	0.7909	0.6200	0.2995	0.1785	0.3325	0.5326	0.5477	0.4981	0.1903	0.1038	0.3846
	$d = 0.30$	1.7247	1.2689	0.8477	0.2023	0.1201	0.2894	0.5431	0.7040	1.0687	0.0944	0.1081	0.3644
	$d = 0.40$	1.7730	0.9028	0.5035	0.0484	0.0779	0.2094	0.2802	2.7237	3.2316	0.1501	0.0895	0.2959
	$d = 0.45$	1.2441	0.4705	0.2074	0.0797	0.0434	0.1563	1.6641	7.9383	6.3409	0.5444	0.1619	0.2445
	$d = 0.49$	0.5274	0.2064	0.0101	0.0356	0.0081	0.0893	27.8318	40.2862	12.9751	21.1537	0.9525	0.1520
n=250	$d = 0.10$	0.1745	0.1788	0.1769	0.0827	0.0276	0.1551	0.1617	0.1630	0.1636	0.0641	0.0350	0.1625
	$d = 0.20$	0.2364	0.2456	0.2034	0.1306	0.0469	0.2052	0.2957	0.3480	0.3665	0.1395	0.0876	0.2263
	$d = 0.30$	0.1102	0.0792	0.0234	0.0135	0.0114	0.1500	0.4727	0.5102	0.3609	0.0510	0.0746	0.1718
	$d = 0.40$	0.0539	0.0145	0.0322	0.0112	0.0212	0.0990	0.7050	0.7941	0.3115	0.0938	0.1889	0.1306
	$d = 0.45$	0.0233	0.0083	0.0067	0.0182	0.0098	0.0689	0.7179	1.9516	0.3862	0.2938	0.5737	0.1137
	$d = 0.49$	0.0111	0.0090	0.0074	0.0037	0.0060	0.0327	3.9296	17.2638	2.6321	2.4971	7.1515	0.0579
n=500	$d = 0.10$	0.1381	0.1408	0.1289	0.0608	0.0104	0.1226	0.1477	0.1527	0.1411	0.0636	0.0463	0.1403
	$d = 0.20$	0.1380	0.0958	0.1079	0.0558	0.0084	0.1038	0.2759	0.2332	0.2562	0.0761	0.0987	0.1267
	$d = 0.30$	0.0439	0.0190	0.0108	0.0119	0.0118	0.0573	0.1888	0.1123	0.0929	0.0146	0.0384	0.0644
	$d = 0.40$	0.0160	0.0021	0.0217	0.0021	0.0107	0.0494	0.0478	0.0527	0.0437	0.0586	0.0433	0.0734
	$d = 0.45$	0.0059	0.0037	0.0042	0.0046	0.0045	0.0415	0.1104	0.1147	0.0654	0.1692	0.0587	0.0744
	$d = 0.49$	0.0024	0.0018	0.0027	0.0020	0.0025	0.0158	0.6217	3.3194	0.8432	1.1082	2.1374	0.0388
n=1000	$d = 0.10$	0.1119	0.1027	0.1132	0.0524	0.0114	0.0949	0.1344	0.1299	0.1362	0.0650	0.0484	0.1137
	$d = 0.20$	0.0574	0.0511	0.0348	0.0192	0.0100	0.0373	0.1308	0.1233	0.1616	0.0414	0.0620	0.0407
	$d = 0.30$	0.0127	0.0118	0.0116	0.0014	0.0013	0.0303	0.0105	0.0286	0.0403	0.0101	0.0106	0.0347
	$d = 0.40$	0.0014	0.0005	0.0019	0.0003	0.0027	0.0216	0.0107	0.0111	0.0370	0.0073	0.0110	0.0314
	$d = 0.45$	0.0036	0.0011	0.0014	0.0019	0.0010	0.0148	0.0167	0.0090	0.0557	0.0233	0.0185	0.0356
	$d = 0.49$	0.0019	0.0020	0.0025	0.0010	0.0015	0.0078	0.0159	0.9528	0.3448	0.3720	1.6849	0.0249